Indian Summer Monsoon variations and competing influences between hemispheres since ~35 ka recorded in Tengchongqinghai Lake, southwestern China

Jie Peng[1], Xiaoqiang Yang[1]*, Jaime L Toney[2]*, Jiaoyang Ruan[1], Guanhua Li[1], Qixian Zhou[1], Huahong Gao[1], Yixuan Xie[1], Qiong Chen[1], Tingwei Zhang[1]

School of Earth Science and Engineering/Guangdong Provincial Key Laboratory of Geodynamics and Geohazards, Sun Yat-sen University, Guangzhou, 510275, China;

2. Geographical & Earth Sciences, University of Glasgow, +44 (0)141 330 6864, UK

E-mail: eesyxq@mail.sysu.edu.cn

Abstract

The southwestern Yunnan Province of China, which is located at the southeastern margin of the Tibetan Plateau and close to Bay of Bengal, is significantly influenced by the Indian Summer Monsoon (ISM). In this study, we reconstruct proxies for the ISM from 35 to 1 ka through detailed analysis of grain-size distribution, geochemical composition and environmental magnetism from a 7.96 m sediment core from Tengchongqinghai Lake, Yunnan Province, China. Globally recognized, abrupt climatic events, including Heinrich Events 0-3 (H0-H3) and the Bølling-Allerød (B/A) warm period are identified in most of our proxies, and the long-term trend is consistent with other published records such as stalagmite oxygen isotopes ($\delta^{18}O$) from Sangxing Cave. Northern Hemisphere (NH) temperature, which

is influenced by NH solar insolation, is commonly suggested to play a dominant role in controlling the ISM. A comparison of our record with the $\delta^{18}O$ variations of ice cores from Greenland and Antarctica, a sea surface temperature (SST) record from the Bay of Bengal, and summer solar insolation at 25^{o}N latitude demonstrates that the general pattern of ISM change does follow variations in summer insolation; however, the ISM lags summer insolation by thousands of years. While the ISM fluctuations are highly correlated with NH temperature on shorter timescales (centennial-millennial), the gradually weakened ISM from 22.5 ka until the Last Glacial Maximum（LGM) indicates a close relationship with the rise of Southern Hemisphere (SH) temperature and the relatively cold background of the SH. Our record expands on the findings of ISM records from Heqing paleolake basin in southwestern China and the Arabian Sea sediments, suggesting that the NH and SH have a competitive influence on ISM by controlling the cross-equatorial pressure gradient. This relationship means that when NH temperatures are relatively high, it has a stronger influence on the ISM than SH influences. In contrast, when the SH temperature is relatively low, it has a dominant influence on ISM. In addition, we speculate that the change of SH temperature not only influences the cross-equatorial pressure gradient directly, but also likely modulates the circulation system of ocean energy by influencing the Atlantic Meridional Overturning Circulation (AMOC).

Key Words: Lacustrine sediment; Indian Monsoon; Lake level; Chemical weathering; Southern Hemisphere.

1. Introduction

The Indian summer monsoon (ISM) is one of major component of the Asian monsoon system, it responds to the hydrology and energy circulation of the coupled atmosphere–ocean–land system and in turn plays a significant role in the global climate (Clemens, 1988; An et al., 2011; Caley et al., 2013; Rosales et al., 2014). Numerous high-resolution paleoclimatic records from natural lacustrine and oceanic sediments and cave deposits have revealed the origin, forcing mechanism and evolution of the ISM over the last 20 years (Fleitmann et al., 2003; Clemens and Prell, 2003; Zhang et al., 2004; Hu et al., 2005, 2007, 2015; An et al., 2011; Deplazes et al., 2013; Rosales et al., 2014; Xiao et al., 2014; Chen et al., 2014; Wang et al., 2015; Wu et al., 2015; Xu et al., 2015; Zhang et al., 2015, 2017). These records suggest that on the glacial-interglacial time-scales, solar insolation of the NH has played the dominant role in the ISM development by controlling the NH temperature (Clemens et al., 2003; Deplazes et al., 2013; Wang et al., 2014; Xiao et al., 2015). In addition, SH temperature has also been suggested to influence monsoon variability by controlling the high-pressure source of the cross-equatorial pressure gradient system in the glacial period, but evidence for this remains scarce (An et al, 2011; Caley et al., 2013). On millennial and centennial time-scales, North Atlantic cold events are implicated in abrupt ISM variations by influencing the AMOC, which has global ocean-air energy links and could affect the location of ITCZ (Alley et al., 1997; Clemens et al., 2003; Hong et al., 2005; Dah et al., 2005; Yancheva et al., 2007; Ziegler et al., 2010; Deplazes et al., 2013). The influence of the SH on millennial time-scales, however, is not well-studied. Interhemispheric temperature and precipitation, especially in the period of global climate fluctuations (such as Heinrich events and Dansgaard-

Oeschger (D-O) events) show an inverse relationship between the NH and SH (Blunier and Brook, 2001; Barker et al., 2009; Pedro et al., 2011; Jo et al., 2014), which is called the "bipolar see-saw" pattern (Blunier, et al., 2001). These phenomena mean that SH climate also influences the ISM by regulating the teleconnections of the global ocean and atmosphere circulation system (Xue et al., 2004; Chiang et al., 2005; Anderson et al., 2009; Gent 2016; Marzocchi and Jansen, 2017). However, the specific influence mechanism needs to be clarified further by additional ISM archives.

Southwestern China, located to the southeast of the Himalayan Mountains, is the key region of the ISM influence of China. The temperature and precipitation of this area are strongly affected by the dynamics of the ISM (An et al., 2011; Chen et al., 2014; Cai et al., 2015; Xiao et al., 2015). Previous paleoclimatic reconstructions of this region using lacustrine sediments and stalagmites showed that the ISM has experienced different stages since the late Pleistocene (Zhang et al., 2011; Xiao et al., 2014; Chen et al., 2014; Wang et al., 2015; Wu et al., 2015; Xu et al., 2015; Zhang et al., 2015, 2017). In addition, the globally recognized periods, such as, the Last Glacial Maximum (LGM) and abrupt millennial or centennial scale climatic fluctuations, such as the Bølling-Allerød interstadial (B/A), Heinrich events (H1-H4) have been identified (Xiao et al., 2014; Chen et al., 2014; Wang et al., 2015; Wu et al., 2015; Xu et al., 2015; Zhang et al., 2015, 2017).

Because most of these previous studies cover relatively short time periods, long, continuous records from appropriate geographical regions are needed to comprehensively understand controls and processes specific to the ISM. Moreover, the combination of multiple climate proxies will help solve the limitations of interpretations based on single proxies (Deplazes et al., 2013; Calay et al., 2013). Two previous studies have reconstructed paleo-fire history and ecosystem hydroclimate

variations of southwestern China from Tengchongqinghai Lake (TCQH) over the past 18 ka and 15.8 ka, respectively (Xiao et al., 2015; Zhang et al., 2015, 2017; Yang et al., 2016). These studies indicate that TCQH sediments are the ideal archive for ISM study, because it has a stable catchment and is uniquely sensitive to ISM variability. Therefore, a longer sediment core, QH4, was drilled in 2014. Here, we present the high-resolution paleoclimate study of QH4 based on grain-size distribution, major geochemical composition, and environmental magnetism over circa the last 35 cal ka BP. This exceptionally long and continuous record allows for the reconstruction of the ISM evolutionary history and determine the competing NH and SH forcing mechanisms related to the ISM.

2. Regional setting

Lake TCQH (25°08′06″-25°07′44″N, 98°34′11″-98°34′26″E; elevation ca. 1850 m) is situated in Tengchong County, Yunnan province, southwestern China (Fig. 1). It is a crater lake with a surface area is about 0.25 km^2. The average water depth is 5.2 m while the maximum water depth was 8.2 m in 2013; The lake is surrounded by hills with the relative altitudes of 120-200 m and 60-140 m on the east and west sides, respectively. In the south-east direction, the gently increased terrain provides the most of deposition detritus. There isn't any external river which brings stable input, the sediments all come from the surrounding small hills and the total catchment area is only about 1.5 km^2. As a result, the lake is sensitive to the hydroclimate of this region. The bed-rocks in the catchment consist of andesite, basalt and tuffaceous breccia. The top soil is about 1-2 m in thickness covered with plenty of vegetation.

Located at the southeastern edge of the Tibetan Plateau and western Gaoligongshan Mountain (Wang et al., 2002), the moist wind from the Arabian Sea

and Bay of Mengal could bring abundant rainfall to fed the lake in summer just as the modern atmospheric observations indicated as Fig. 1 shows. However, the winter monsoon less affects the lake as the blocking of Gaoligongshan Mountain. The annual average temperature is about 15.9℃ and annual precipitation is about 1492 mm. As Fig. 2 shows, Tengchong actually has a typical monsoon climate, about 75% of precipitation is supplied between May and September. Therefore, the sedimentation of TCQH could reliably record the evolution history of the ISM.

3. Material and methods

3.1. Sampling

In 2014, a 16.96 m long sediment core, QH4 (25°7.871' N, 98°34.388' E), was drilled to the bed rock in a water depth of 2.13 m using a gravity piston corer in northeast of TCQH basin. In this paper, we focus on the depth interval of 0.21-7.96 m in the core. We chose this interval because the upper 0.21 m section was disturbed by fishing activities and the section below 7.96 m lacks chronological references for dating. The sediments of core composed mainly of grey-black clayey silt with the variant color in the different layer. Following is a brief introduction to the section from the top to the bottom:

a. 0-3 m, Dark grey clayey silt with rich organic content;

b. 3-3.8 m, Gray-black clayey coarse silt dotted with fine sand;

c. 3.8- 5.24 m, Dark gray to light brown clayed silt dotted with a little of gray-green volcanic ash spots;

d. 5.24-5.68 m, Colorful volcanic ash deposits or rapid runoff sediments comprising of silt, fine sand and small gravel with less organic content;

e. 5.68-6.06 m, Dark silty clay with high organic content;

f. 6.06-6.65 m, Light brown yellow silty clay;

g. 6.65-7.96 m, Light gray-black silty clay stained with a little of offwhite or light blue ash spots.

One half was continuously sampled by pushing plastic cubes (2×2×2 cm^3) into the split face of the core sections for environmental magnetism analysis, and a total of 276 samples were obtained. The remaining half was also sliced continuously at 2 cm intervals. and the samples were freeze-dried for the other analyses.

3.2. Methods

The chronology of the core was established with accelerator mass spectrometer radiocarbon ^{14}C (AMS ^{14}C) dating of nine plant remains (tree branches or leaves) and four bulk sediment samples, which were analyzed at Beta Analytic Testing Laboratory, USA. The conventional AMS ^{14}C ages were calibrated using the $CALIB_{702}$ program (IntCal13 data set, Reimer et al., 2009). The age-depth model was established using Bacon software (Blaauw and Christen, 2011). Grain-size analysis of all samples was performed using a Malvern Instruments Mastersizer-3000 at Sun Yat-Sen University for all sample. Prior to measurement, organic matter and carbonate were removed using 10% H_2O_2 and HCl, respectively. The grain size data was analyzed using Malvern software and following the methods suggested by Simon et al (2001) and Qin et al. (2005) respectively at last. Geochemical major elemental concentrations were measured at 8 cm interval using an X-ray fluorescence spectrometer (XRF, Rigaku ZSX Primus-Ⅱ) at Sun Yat-Sen University. The carbonate content was removed using 10% HCl. Then the samples were hand-milled

by the agate mortar and prepared for analysis after sieving through a 250 mm sieve. Firstly, the sample was ignited in muffle furnace for 2 h at 900 ℃. Then the baked sample was fused with a 2:1 mix of lithium tetraborate and lithium metaborate, at 1050 ℃ for 20 minutes, to form a glass bead for test. The chemical weathering index CIA is defined as $Al_2O_3/(Al_2O_3 + CaO^* + Na_2O + K_2O)\times100$, where CaO* indicates the calcium content in the silicate fraction of the sediments (Nesbitt and Young, 1982). Magnetic susceptibility-Temperature measurements (χ-T curves) for representative four samples were measured in the Institute of Geology and Geophysics, Chinese Academy of Sciences. Analysis was performed in an argon atmosphere using an AGICO MFK1-FA equipped with CS-3 temperature control system and with temperature ranging from 25℃ to 700℃ with a ramping rate of 2℃/min in this study. Environmental magnetic measurements for the all samples were performed on the 276 samples in the Institute of Geology and Geophysics, Chinese Academy of Sciences. The low-field magnetic susceptibility (κ) was measured using a Bartington MS2 meter with the frequency at 470 Hz. Isothermal remanent magnetization (IRM) was induced with direct current (DC) fields of 1T and -300 mT with a 2G Enterprises model 660 pulse magnetizer, the saturation IRM (SIRM) and IRM_{-300mT} were measured using a 2G-760 IRM system. S-ratio is defined as the ratio of IRM_{-300mT} to SIRM (King and Channell, 1991) for estimating the relative contributions of low-coercivity magnetic minerals, with the "hard" fraction of IRM (HIRM) defined as 0.5 × (IRM_{1T} + $IRM_{-300\ mT}$) (Thompson and Oldfield, 1986), which is oppositely indicated by the absolute concentration of high-coercivity magnetic minerals. Anhysteretic remanent magnetization (ARM) was produced in an alternating field of 80 mT peak field superimposed over a 0.05 mT DC field using a 2G-760 ARM system. Ten typical samples with high coercivity based on the HIRM data were chosen for

188 measurement of the diffuse reflectance spectrophotometry (DRS) (Deaton and Balsam,
189 1991) using the Perkin Elmer spectrophotometer in Sun Yat-Sen University. The
190 selected samples were evenly coated on the glass with the distilled water and scanned
191 from 400 to 700 nm in 0.50 nm steps after being dry naturally.

192 # 4. Results

193 ## 4.1. AMS ^{14}C dating result

194 As shown in Table 1, the age of the bottom sediments is 35.08 ± 0.38 cal ka B.P.
195 and the average sediment accumulation rate is about 4.5 ka/m. There is one specific
196 abnormal, non-laminated section from 5.24 m to 5.73 m, where the dominant
197 composition is gray tufa masses of irregular grain-size. We speculate that it might
198 have been washed into the lake abruptly or come from a volcanic eruption within a
199 short time, so we take the average value of all the proxies of the 49 cm section as one
200 representative sample, which avoids misrepresentation of the sediment rate and time-
201 depth relationship.

202 ## 4.2. Grain-size and geochemical major elements results

203 Generally, grain size distributions of samples display unimodal or bimodal
204 (Suppl. 1), poorly sorted. The mean grain size (using the FOLK and WARD method
205 (Blott & Pye, 2001)) varied around 9.04 μm (std.=3.77) , the skewness and kurtossis
206 were characterized with the mean values -0.055 (std.=0.071) and 0.998 (std.=0.065),
207 respectively. The bimodal and little positive skewness just mainly occurred between
208 the 29-33 ka, corresponding to the larger sorting values. The fraction of very fine silt
209 and clay (<4 μm) contributes the component of about 27.3%. Three independent

components can be separated for all samples (Qin et al., 2005). The size of the first component is generally less than 1.3 μm, and the second predominant component distributed within the size of 1.3-63 μm with varied median grain size from 5 μm to 15 μm; the size of the third component is mainly between 63 and 1000 μm. The grain fraction of <1.3 μm, 1.3-5 μm (FGS) and 1.3-15 μm show an agreement pattern, which is opposite to the variations 63-1000 μm (Figure 4). A series of climate events, such as cold events H0-H3 and warm event B/A can be recognized by low FGS fraction and relative high coarse fraction (Hemming & Sidney, 2004). The proportion of grain size from 1.3 to 5.0 μm (FGS), the gradually increased part possessing a mean fraction 29% in the second component defined by two inflexion, which is more sense to the relative level fluctuations, roughly relating to the less sorting values. The grain size distribution along with the time scale can be divided into five stages:

First stage (a, 35-29 ka), FGS varied from a high content to relative low, corresponding the coarse grain fraction increase rapidly, which may arise from the contributions of volcanic detritus influx. The second stage (b, 29-19.2 ka) displays a gradually decreasing trend, and third stage (c, 19.2-15 kyr) possesses of the lowest vale, linking to the LGM period. The consequent fourth (d, 15-6.2 kyr) and fifth (e, 6.2-1 kyr) stages have again increased and then reduced fine fraction. Every stages are all punctuated with several significant narrow low vales and high peaks, presenting some rapid events.

The XRF results show the variations very similar to the fine grain size fraction (Figure 5). The high contents of TiO_2, Al_2O_3 and the ratio of Fe_2O_3/CaO_2, TiO_2/CaO_2 as well as the CIA index are close related to the high FGS fraction, and vice vesa. However, the sampling resolution are less than the particle analysis, thus missing some climate events information.

4.3. Rock magnetic and environment magnetic results

The κ-T curves of the typical samples substantially decrease during the 550-600 ℃ portion of the heating process, which demonstrates the thermal unblocking of major magnetic mineral-magnetite, as shown in Figure 6. There is a slightly decreasing trend after 600℃ as well, which usually indicates the presence of hematite. The obvious hump between 450 to 550 ℃ is probably the result of the neo-formation of magnetite transformed from iron-containing minerals such as silicates, clays or carbonates (Deng et al., 2001). The second derivative curves of DRF are shown in Figure 7, their characteristic bands center at about 450 nm and 580 nm, indicating goethite and hematite, respectively (Deaton and Balsam, 1991).

The volume susceptibility (κ) of most samples is relatively weak (with an average value of 2.2×10^{-5} SI) and all samples above the depth of 0.73 m are negative (close to zero, not shown), arising from the high organic content. The other concentration-dependent magnetic parameters, e.g. SIRM and ARM, have similar variations with the κ throughout the whole sequence.

S-ratio values of almost all samples are high (with an average value of 0.91), suggesting that values are controlled by the low-coercivity magnetic mineral magnetite. However, it is the high-coercivity magnetic mineral which give rise to the change of SIRM, κ and ARM throughout the whole sequence as HIRM being consistent with SIRM, κ and ARM, but not the S-ratio as shown in Figure 8.

5. Discussion

5.1. Environmental significance of the proxies

A series of investigation results present that the particle size in a closed lake can serve as a proxy indicating the lake level fluctuation (Qin et al., 2005; Zhang et al., 2017; Li et al., 2017). The proportion of fine grain (<16 μm) in the center of lake is clearly larger than that in the margin for the surface sediments (Zhang et al., 2017; Li et al., 2017). At the same site, the increasing fraction of fine grain along with the depth raised from rising lake level. TCQH lake is enclosed by small hills without other water system influx and outflow, and the deposition particles are mainly produced from the detrital materials by weathering base rock around the hills. Therefore, the grain-size can be viewed as an indicator of lake level, owning the grain-size of the sediments would progressively become smaller with the extended distance from the shoreline (Zhang et al., 2017). This is confirmed by previous detailed grain-size analysis of surface sediments from TCQH, where the small grain-size fraction (<16 μm; SGS) gradually increases from ~35% to ~65% with increasing lake water depths from ~2 m to ~6.5 m (Zhang et al., 2017). Therefore, the high percentage of SGS in certain site could indicates the periods of high lake level, and vice versa. As the nature rainfall controlled by the ISM consist of water source of TCQH lake, the gain-size change can also indicate the variation of the ISM strength indirectly.

As the hills surrounded the TCQH lake were formed by volcanic rock, the geochemical elements and magnetic minerals all come from the chemical weathering process. The weathering intense and the detritus influx are reasonably influenced by the precipitation (White & Blum, 1995). Enhanced effective precipitation and warm

climate would produce more plentiful detritus and transport to the lake. The well consistent between the contents of TiO_2, the ratio of Fe_2O_3/CaO and TiO_2/CaO, CIA index and magnetic proxies of SIRM, HIRM as well as the high fraction of fine grain, denote the commonly controlling factors. CIA is a well-established indicator of chemical weathering strength based on the fact that the major elements behave differently during the weathering processes (Nesbitt and Young, 1982). In addition, the ratios of major elements also have been widely used as the proxy of weathering (Sun et al., 2010; Engstrom and Wright, 1984). Following this principle, high TiO_2 and Al_2O_3 content, high ratios of TiO_2/CaO, Fe_2O_3/CaO and CIA indicate a strong ISM. The environmental magnetism parameters κ, ARM and SIRM are usually indications of magnetic mineral concentrations, and ARM is particularly sensitive to the stable single domain (SD) ferromagnetic particles (Maher, 1988; Hu et al., 2005). SIRM reflects the concentration of remanence carriers (ferromagnetic and antiferromagnetic particles). These proxies show strong correspondence throughout the core, suggesting that they are not greatly influenced by mineralogy and grain-size of the magnetic minerals (Liu et al., 2016). As the magnetic minerals originate from the weathering of exposed bedrock and surface soils in the catchment, their concentrations also reflect the weathering intensity and transporting capacity of runoff. DRF results indicate that goethite and hematite are the hard magnetism fraction of samples with high HIRM values. Commonly, iron oxidation requires an electrolyte, such as water (Davison and Seed 1983). Thus, the high HIRM correspond to a highly moisture environment with the strong ISM (Jiang et al., 2016; Hu et al., 2015). Besides, magnetic dissolution is ubiquitous in suboxic and anoxic environments (Liu et al., 2000; Duan et al., 2014). Thus, the high organic content would result in an environment supportive of dissolving magnetic minerals (especially SD ferrimagnetic

particles) (Nowaczyk et al., 2002; Duan et al., 2014), but enhanced oxygen concentration caused by wind could increase preservation of magnetic minerals, so strong ISM is benefit to both the production and preservation of magnetic minerals.

As illustration above, the fraction of fine grain suggests the lake level fluctuation, and chemical elements as well as its ratios accompanied with magnetic parameters influenced by the effective precipitation, weathering process and detritus influx. We processed the PCA analysis using CANO software for fine grain fraction， ARM/SIRM, SIRM, HIRM and the content of TiO_2, the results show that they are distributed in one quadrant, denoting the similar dominating climate factors. They can serve as the proxies of ISM.

5.2. Paleoclimate changes since the late last glacial period

Based on the signals from all paleoclimate proxies in this study, the period between 35-1 ka BP could be divided into 5 intervals (a-e) from bottom to top as shown in Fig. 4-5 and Fig. 8. Notably, there are significant ISM strength excursions during the periods of 32-29.8 ka BP, 15.8-15.2 ka BP, 14.7-14.2 ka BP, 8-7.5 ka BP, respectively.

In interval a (35-29 ka BP), the rich chemical elements, such as Al_2O_3, TiO_2, CIA and high magnetic assemblage indicate that the strong ISM enhanced the chemical weathering and resulted in more elements and magnetic minerals being transported into the lake. High fine grain fraction also indicates higher lake level. This is consistent with a sediment record in Xingyun Lake, which is 500 km away from TCQH. The highest percentages of pine forest and evergreen broadleaved forest

(dominated by evergreen *Quercus*) as well as the lowest percentages of mean grain-size both imply a relatively high lake level, which is the wettest period in the whole record from 36.4-13.4 ka BP (Chen et al., 2014; Wu et al., 2015). In addition, ISM strength declined significantly during the period of 31.95-29.8 ka BP, which might correspond to the global cold event Heinrich 3 (Broecker et al., 1992).

In interval b (29-19.2 ka BP), the elements, magnetic concentration and FGS content gradually decreased, showing a gradual weakening ISM trend.

In interval c (19.2-15 ka BP), this period can be recognized as the Last Glacial Maximum (LGM) characterized by the minimal major minerals, magnetic minerals and FGS since 35 ka BP.

In interval d (15-6.2 ka BP), the B/A warm event is shown by the remarkable increase of FGS fraction, SIRM and ARM. This event terminated the weakest ISM period (LGM) and began the strong ISM period until ~6.2 ka BP. During 7.8-8 ka BP, the Al_2O_3, TiO_2, SIRM show a slight fluctuation, which might correspond to the 8.2 ka cold event (Alley et al., 1997). However, the famous cold event YD is shown only in the grain-size below 16 μm.

In interval e (6.2-1 ka BP), the values of Al_2O_3, TiO_2, CIA, κ, ARM and SIRM are relatively low, indicating the weakening ISM since 6.2 cal ka BP. This is the popular milestone in Holocene climate change, which is also recorded in other ISM regions, such as the Bay of Bengal (turning at about 5 ka BP, Rashid et al., 2011) and Lahaul Himalaya (turning at about 5.77 ka BP, Rawat et al., 2015).

5.3. Comparison between regional climate history

The topography in Fig. 1 shows that the altitude along the path of the ISM (from

351 the Bay of Bengal to TCQH) is gradual increased, indicating that the ISM is a major
352 climate driver in the TCQH catchment. To further confirm the reliability of our
353 record, we compared them with the previous TCQH study results (Fig. 9B and Fig.
354 9C, Zhang et al., 2015, 2017) and other available records from the ISM region. In
355 particular, records from southwestern China, such as stalagmite $\delta^{18}O$ from
356 Xiaobailong Cave (Fig. 9A, Cai et al., 2015), geochemical minerals parameters K/Rb
357 from Baoxiu peat (Fig. 9D, Huang et al., 2016), pollen percentage of cold tolerant
358 conifers from Xingyun Lake (Fig. 9 E, Chen et al., 2014), stalagmite $\delta^{18}O$ from
359 Sanxing Cave (Fig. 9F, Jiang et al., 2014) and Arabian Sea sediment reflectance L*
360 (Fig. 9I, Deplazes et al., 2013) provide good comparators. As a whole, although the
361 time span and resolutions of these records are not completely coincident, the overall
362 trend and most distinct features are similar.

363 As Fig. 9 shows that the general trend of the stalagmite $\delta^{18}O$ record from
364 Sanxing Cave is the most similar to SIRM of QH4 among the all regional records.
365 The Sanxing $\delta^{18}O$ values increased from the most negative -8.1 ‰ to -6.0 ‰
366 gradually from 30.9 to 17 ka BP (Jiang et al., 2014), which is consistent with the
367 decline in SIRM of TCQH. Although different climatic proxies were used and the
368 distance between TCQH and Sanxing Cave is 500 km, they both shown the
369 decreasing strength of the ISM from 30 to 17 ka BP. In conclusion, although there are
370 differences in the latitude, elevation, distance to sea, topography and geomorphology
371 of different ISM records, which have an inevitable impact on their climate (Clemens

et al., 2003), most of the records indicated the ISM was persistently decreasing during 30 to 17 ka BP.

5.4. Global correlations and the forcing of the ISM

Multiple lines of evidence indicate that NH temperature, controlled by the solar insolation, dominated the ISM evolution by influencing the migration of the ITCZ (Fleitmann et al., 2003, 2007; Deplazes et al., 2013; Xiao et al., 2014; Huang et al., 2016). Meanwhile, ISM events also correspond to North Atlantic ice rafted debris (IRD) events in most records (Schulz et al., 1988; Gupta et al., 2003; Ziegler et al., 2010; Deplazes et al., 2013). In addition, Zhang et al. (2017) suggests that the migration of ITCZ induced by solar insolation alone cannot account for the Holocene hydroclimate fluctuations of the eastern ISM domain. The large-magnitude fluctuations from 5 to 4 cal ka BP recorded by TiO_2 and grain-size in TCQH reveal the close links to the Arabian Sea sea-surface temperature (SST) and the ISM strength variations. Briefly, continental drainage could affect surface ocean conditions of the Andaman Sea and Bay of Bengal. In turn, slight increases in ocean SSTs might enhance moisture exchange from the ocean to the atmosphere and the enhanced moisture of atmosphere would then be transported to South Asia and southwestern China by the ISM. In other words, the ISM is subjected to complex influences from external and internal climate forcing, and in return, plays an important part in driving global air and energy systems (Caley et al., 2013; Rosales et al., 2014).

As we know, the ISM is formed from the cross-equatorial pressure gradient between the low atmosphere pressure (Indian low) over the Asian landmass and high pressure (Mascarene High) over the subtropical Indian Ocean (Clemens et al., 1998; Caley et al., 2013; Hong et al., 2005; An et al., 2011). Therefore, the lower the Indian

Low and/or the higher the Mascarene High, the stronger the intensity of the ISM. However, most previous studies of the ISM concentrate on changes in NH conditions that are influenced by only the Indian Low (Clemens et al., 2003; Wang et al., 2014; Xiao et al., 2015). One of major reasons for this is the lack of climate archives with high-resolution and dating certainties from the SH (Weber et al., 2014). In fact, even though NH temperature and large-scale climate events might dominate the ISM evolution, the influence coming from the SH is needed to further explore the "bipolar see-saw" connection between the climate of the NH and the SH (Blunier and Brook, 2001; Knutti et al., 2004; Jo et al., 2014). For example, the atmospheric methane records from the Greenland Ice Sheet Project 2 (GISP2) ice core and Antarctica Byrd ice core show that the onset of seven major millennial-scale warming events between 90 to 10 ka in Antarctica preceded the onset of Greenland warming events by 1.5 to 3 ka (Blunier and Brook, 2001). A stalagmite record from Korean Peninsula (in the NH) and Naracoorte, Southeastern Australia (in the SH) over the past ~550 ka also show an inter-hemispheric, hydrologic see-saw that extended to mid-latitudes from peak interglacial to mid-sized glacial periods (Jo et al., 2014). It is also generally accepted that climate variability in the NH is usually accompanied by temperature changes in Antarctica that is coupled through ocean thermohaline circulation (Knutti et al., 2004). We have sufficient evidence to infer that there must be a mechanistic link between the ISM and SH climate, which is related to the change of Mascarene High and/or Indian Low, either directly and/or indirectly.

We specifically compare our SIRM and FGS (grain-size 1.3-5 μm) records with the $\delta^{18}O$ record of the GRIP2 ice core from Greenland (Grootes et al., 1993), average summer insolation at 25°N (Laskar et al., 2004), the SST reconstruction from core SK218/1 collected from western Bay of Bengal (Govil and Naidu, 2011), and the $\delta^{18}O$

record from the ice core from European Project for Ice Coring in Antarctica (EPICA) in the Dronning Maud Land (EDML) (EPICA community members, 2006) (Fig. 10). We use these records below to supplement our new data and to explore the driving force (s) of the ISM since 35 cal ka BP by systematic and comprehensive analyses.

5.4.1. Long-term ISM evolution driven by summer insolation

Comparing proxies of QH4 with NH summer insolation indicates that the insolation provides the major forcing of ISM change, but there is an obvious lag of the ISM behind the insolation. We mainly focused on the weakest ISM of the QH4 record in about 15 ka. As Fig. 10 shows, the ISM change lags about 7 ka behind the weakest summer insolation at 25°N in 22 ka, just as the previous Arabian Sea sediment record indicated. It is shown that maximum summer surface water productivity of Arabian Sea lagged the precession-related maximum solar insolation by about 6 ka, which was suggested to be related to the cross-equatorial transport of latent heat (Reichart et al., 1998; Clemens et al., 2003).

5.4.2. Remarkable ISM fluctuations relate to bipolar temperature

Six strong millennial-to-centennial ISM peaks (a, b, c, d, e, f) occur in the QH4 SIRM and FGS curves and are consistent with the more positive $\delta^{18}O$ values of the GRIP2 ice core and the more negative $\delta^{18}O$ values of EDML ice core within the age uncertainties from 35-26 cal ka BP. The fluctuations of GRIP2 and QH4 records are remarkably sharper than EDML $\delta^{18}O$ record, while the SH temperature revealed relatively mild and cold conditions in this period. Based on these correlations, the ISM strong events are likely influenced by the temperature of the NH and SH together, but the NH played a leading role during this period. Notably, the increase of the SST

in the Arabian Sea from 30 to 26 cal ka BP did not strengthen the ISM.

5.4.3. ISM weakening influenced by SH temperature

The most outstanding feature of the ISM indicated by SIRM and FGS is the gradual weakened trend of ISM from 27 to 17.5 cal ka BP. However, what is worth noting is that this gradual weakening trend occurred, despite the fact that the NH temperature was rising from 22.5 to 19.2 ka. This means that the rising NH temperature did not strengthened the ISM intensity at this time. Surprisingly, SH temperature gradually increased from 27 to 14 ka, albeit more mildly before 18 ka. It appears that the SH exhibited a more important influence on the ISM by weakening the pressure gradient during this time. In addition, both NH and SH temperatures were relatively low throughout this time. The statistical test between Arabian Sea productivity records and bipolar climate records (NGRIP and EDML ice $\delta^{18}O$) in the interval of 40-16 ka also reveals a better correlation between Arabian Sea Br (a proxy for marine productivity) and EDML $\delta^{18}O$ records than NGRIP $\delta^{18}O$ records (Caley et al., 2013). Synthesizing the ISM record characteristics from 35 to 27 cal ka BP, we suggested that the SH does not play a significant role in controlling the ISM compared to the NH when the NH has relatively higher average temperatures. Whereas, the converse is true, that when the SH has lower temperatures, it has a stronger impact on the ISM than the NH. This rule is not only confirmed by the Arabian Sea Br records, but also is consistent with the Heqing Basin ISM proxies (weathering proxy (Rb/Sr) and biologic productivity proxy (TOC) at glacial-to-interglacial time-scales. Since 2.60 Ma, ISM minima occurred 14 to 35 ka earlier than the timing of NH glaciation maxima during the transition from interglacial into glacial. As a result, the ISM was slowly strengthening coeval with increasing NH glaciation, at the same time that SH

468 temperature was nearly at its lowest and Antarctic ice volume was increasing (An et
469 al., 2011). An et al. (2011) attribute the glacially strengthened ISM to the strong SH
470 atmospheric meridional circulation and intensified Mascarene High as a result of low
471 SH temperature and increased Antarctic ice volume. This pattern suggests that the
472 stage of cold temperatures in the SH is a required background state for influencing the
473 ISM. In fact, as Fig. 10 shows, after the B/A warm period, SH temperature remains
474 relatively high and showed no obvious control on ISM thereafter.

475 For the records of the $\delta^{18}O$ of ice core from EDML, EDC3 and GISP2 (Jouzel et
476 al., 2007; EPICA Community Members, 2006; WAIS Divide Project Members, 2015),
477 and the FGS fraction as well as ARM/SIRM, we further separate them into four
478 primary components (PC1-PC4) using the Singular Spectrum Analysis (SSA) method
479 and carry out the spectra analysis with PAST software respectively (Hammer et al.,
480 2001; Ghil et al, 2002) (Supp. 2). It is very clear that the periods ~3.8, ~1.5 and ~1.1
481 ka in grain fraction closely correspond to that those recorded in GISP2, while the
482 periods of ~4.0 ka and 2.5 ka in grain fraction and ARM/SIRM can only find the
483 counterpart in Antarctic records (Supp. 3). The almost consistent pattern of the FGS
484 and ARM/SIRM in the component 3 (PC3) illustrates the similar climate controlling
485 conditions. We compiled them into a synthesizing proxy after normalization, and
486 designated low proxy value as the weak ISM event. Thus, these events can be
487 numbered as 'Q1-Q14'. Almost all the weak ISM events related to the warm Antarctic
488 temperature except of events Q4 and Q6. Same results were proofed by the stalagmite
489 records in central China (Chen et al., 2016). We suppose that the influence of
490 Greenland climate to ISM should be connected by the global conveyor belt, which
491 transport the cold water to Indian Ocean, cooling the surface water and causing
492 weaken ISM; while Antarctic temperature adjust the atmospheric meridional

493 circulation rapidly.

494 5.4.4. How the SH temperature influences in ISM

495 Overall, there are two possible driving mechanisms of the ISM that are related to
496 SH temperature.

497 (1) Atmosphere modulation system

498 It is known that the ISM is controlled by the cross-equatorial pressure gradient,
499 mainly that the low pressure over Asia, which is caused by sensible heating of the
500 Asian land surface and latent heating derives from surface evaporation over Indian
501 Ocean (Clemens et al., 2003), and the high pressure, the Mascarene High, which is
502 closely related to the circumpolar low in high southern latitudes. Relatively low SH
503 temperature could induce great intensification of a high-pressure system over the
504 Mascarene region, and strengthen the cross-equatorial Somali jet as a result of ISM
505 being strengthened (Xue et al., 2004; Caley et al., 2013; Frierson et al., 2013).
506 Whereas, when the SH temperature increases, the ISM will correspondingly be
507 weakened.

508 (2) Ocean-atmosphere system

509 Another driving force for cross-equatorial pressure gradient comes from the
510 ocean-atmosphere circulation system. According to satellite observations and climate
511 model simulations, the Atlantic Meridional Overturning Circulation (AMOC) plays a
512 significant role in heat transport from SH to NH (Frierson et al., 2013). Previous
513 studies show that a massive supply of sea-ice and freshwater in North Atlantic Ocean
514 perturbed surface and deep waters of ocean (Alley et al., 1997; Bard et al., 2000),
515 which led to a change in the AMOC. This in turn influenced the position of ITCZ as
516 the close heat-cycle relationship exists between the AMOC and the ITCZ (Dahal et al.,

2005; Denton et al., 2010; Deplazes et al., 2013; Frierson et al., 2013; Marshall et al., 2014; McGee et al., 2014). In fact, more and more clues are offered by climate simulations and paleoclimate records support that the Antarctic sea ice and temperature could modulate the global climate change (Bintanja et al., 2013), especially by influencing the AMOC and atmospheric carbon dioxide concentrations (Vellinga and Wood, 2002; Barker et al., 2009; Marzocchi and Jansen, 2017).

6. Conclusions

Constrained by thirteen AMS ^{14}C ages, combined multi-proxies, such as geochemical properties (major elements concentration and CIA), geophysical parameters (environmental magnetism and rock magnetism) and lithological variations (grain-size) across the length of 7.76 m sediments core from TCQH, show the ISM evolution history in southwestern China from 35 to 1 cal ka BP.

The results revealed five different stages of ISM evolution in this region: from 35 to 29.8 cal ka BP, the relative strong ISM strength with significant fluctuations; from 29.8 to 19.2 cal ka BP, the overall gradual decreasing of ISM change; from 19.2 to 15 cal ka BP, represent the LGM with weak ISM strength; from 15 to 6.2 cal ka BP, the relative strong ISM strength; from 6.2-1 cal ka BP, the gradual weakening ISM strength again. A series of global climate events are records in our study, including in the North Atlantic 8.2 ka cold event, Heinrich 3 cold event and B/A warming event.

We suggested that both the external solar insolation and internal NH and SH temperature control the ISM evolution by impacting the cross-equatorial pressure

gradient. However, the temperature of NH and SH play the competitive influence in dominating the ISM variability at different stages, either the higher NH temperature than normal or lower SH temperature than normal would have dominated influence in ISM intensity.

Acknowledgments

We thank Zongqi Duan, Shihu Li, Huafeng Qin, Bailing Wu, Jie Yuan and Zhaoxia Jiang (Institute of Geology and Geophysics, Chinese Academy of Sciences) for instruction of magnetic test, Lu Wang, Min Zhou and Fan Yang (Sun Yat-sen University) for their assistance in field and laboratory, and Pat Munday (Montana Tech) for his assistance with technical editing. This project was supported by NSFC (Natural Science Foundation of China; grant no. 41030366 and 41672162) and Guangdong Province Introduced Innovative R&D Team of Geological Processes and Natural Disasters around the South China Sea (grant no. 2106ZT06N331). Finally, we would like to acknowledge the comments and recommendations of the reviewers who helped us to improve the quality of this work.

References

Alley, R.B., Mayewski, P.A., Sowers, T., Stuiver, M., Taylor, K.C., Clark, P.U., 1997. Holocene climatic instability: a prominent, widespread event 8200 yr ago. Geology 25, 483-486.

An, Z.S., Clemens, S.C., Shen, J., Qiang, X.K., Zhang, D.J., Sun,Y.B., Prell, W.L., Luo, J.J., Wang, S.M., Xu, H., Cai, Y.J., Zhou, W.J., Liu, X.D., Liu, W.G., Shi,

Z.G., Yan, L.B., Xiao, X.Y., Chang, H., Wu, F., Ai, L., Lu, F.Y., 2011. Glacial-Interglacial Indian Summer Monsoon Dynamics. Science. 333, 719-723.

Anderson, R.F., Ali, S., Bradtmiller, L.I., Nielsen, S.H., Fleisher, M.Q., Anderson, B.E., Burckle, L.H., 2009. Wind-driven upwelling in the Southern ocean and the deglacial rise in atmospheric CO_2. Science. 323, 1443-1448.

Bard, E., Rostek, F., Turon, J.L., Gendreau, S., 2001. Hydrological impact of Heinrich events in the subtropical northeast Atlantic. Science. 289, 1321-1324.

Barker, S., Diz, P., Vautravers, M.J., Pike, J., Knorr, G., Hall, I.R., Broecker, W.S., 2009. Interhemispheric Atlantic seesaw response during the last deglaciation. Nature. 457, 1097-1102.

Bintanja, R., Oldenborgh, G. J., Drijfhout, S.S., Wouters, B., Katsman, C.A., 2013. Important role for ocean warming and increased ice-shelf melt in Antarctic sea-ice expansion. Nature Geosci. 6, 376-379.

Blaauw, M., Christen, J.A., 2011. Flexible paleoclimate age-depth models using anautoregressive gamma process. Bayesian Anal. 6, 457-474.

Blott, S. J., Pye, K., 2001. Gradistat: A grain size distribution and statistics package for the analysis of unconsolidated sediments. Earth Surface Processes and Landforms 26, 1237-1248.

Blunier, T., Brook, E.J., 2001. Timing of millennial-scale climate change in Antarctica and Greenland during the Last Glacial Period. Science. 291, 109-121.

Broecker, W., Bond, G., Klas, M., Clark, E., McManus, J., 1992. Origin of the northern Atlantic's Heinrich events. Clim. Dyn. 6, 265-273.

580 Cai, Y.J., Fung, I.Y., Edwardsd, R.L., An, Z.S., Cheng, H., Leef, J.E., Tan, L.C.,
581 Sheng, C.C., Wang, X.F., Dayc, J.A., Zhou, W.J., Kellyd, M.J., Chiang, J. C. H.,
582 2015. Variability of stalagmite-inferred Indian monsoon precipitation over the past
583 252,000 y. PNAS. 112, 2954-2959.
584 Caley, T., Zaragosi1, S., Bourget, J., Martinez, P., Malaizé, B., Eynaud, F., Rossignol,
585 L., Garlan, T., Zimmermann, N. E., 2013. Southern Hemisphere imprint for Indo-
586 Asian summer monsoons during the last glacial period as revealed by Arabian Sea
587 productivity records. Biogeosci. 10, 7347-7359.
588 Chen, S. T., Wang, Y. J., Cheng, H., Edwards, R. L., Wang, X. F., Kong, X. G., Liu,
589 D. B., 2016. Strong coupling of Asian Monsoon and Antarctic climates on
590 suborbital timescales. Scientific Reports 6:32995, DOI: 10.1038/srep32995
591 Chen, X.M., Chen，F.H., Zhou, A.F., Huang, X.Z., Tang, L.Y., Wu, D., Zhang, X.J.,
592 Yu, J.Q., 2014. Vegetation history, climatic changes and Indian summer monsoon
593 evolution during the Last Glaciation (36,400-13,400 cal yr BP) documented by
594 sediments from Xingyun Lake, Yunnan, China. Palaeogeogr. Palaeocl. Palaeoecol.
595 410, 179-189.
596 Chiang, J.C.H., Bitz, C.M., 2005. Influence of high latitude ice cover on the marine
597 Intertropical Convergence Zone . Cli. Dyn. 25, 477-496.
598 Clemens, S.C., Prell, W.L., 2003. A 350,000 year summer-monsoon multi-proxy
599 stack from the Owen Ridge, Northern Arabian Sea. Marine Geo. 201, 35-51.
600 Dahl, K.A., Broccoli, A.J., Stouffer, R.J., 2005. Assessing the role of North Atlantic
601 freshwater forcing in millennial scale climate variability: a tropical Atlantic

perspective. Cli. Dyn. 24, 325-346.

Davison, W. and Seed, G., 1983. The kinetics of oxidation of ferrous iron in synthetic and natural waters, Geochim. Cosmochim. Acta. 47, 67-69.

Deaton, B.C., Balsam, W.L., 1991. Visible spectroscopy, a rapid method for determing hematite and geothite concentration in geological materials. J. Sedi. Res. 61, 628-632.

Deng, C.L., Zhu, R.X., Jackson, M.J., Verosub, K.L., Singer, M.J., 2001. Variability of the temperature-dependent susceptibility of the Holocene eolian deposits in the Chinese loess plateau: a pedogenesis indicator. Phys. Chem. Earth. 26, 873-878.

Dentón, G.H., Anderson, R.F., Toggweiler, R. F., Edwards, R. F., Schaefer, M., Putna, A.E., 2010. The Last Glacial Termination. Science. 328, 1652-1656.

Deplazes, G., Lückge, A., Peterson, L.C., Timmermann, A., Hamann, Y., Hughen, K. A., Röhl6, U., Laj, C., Cane, M.A., Sigman, D.M., Haug, G.H., 2013. Links between tropical rainfall and North Atlantic climate during the last glacial period. Nature Geosci. 6 (3), 213-217.

Doberschütz, S., Frenzel, P., Haberzettl, T., Kasper, T., Wang, J., Zhu, L.P., Daut, G., Schwalb, A., Mausbacher., 2014. Monsoonal forcing of Holocene paleoenvironmental change on the central Tibetan Plateau inferred using a sediment record from Lake Nam Co (Xizang, China). J Paleolimnol. 51, 253-266.

Duan, Z.Q., Liu, Q.S., Yang, X.Q., Gao, X., Su, Y.L. 2014. Magnetism of the Huguangyan Maar Lake sediments, Southeast China and its paleoenvironmental

623 implications. Palaeogeogr. Palaeocl. Palaeoecol. 395, 158-167.
624 Engstrom, D.R. and Wright, H.E., 1984. Chemical stratigraphy of lake sediments as a
625 record of environmental change. IN: Haworth, E. Y. and Lund, W. G. (eds), Lake
626 Sediments and Environmental History. pp.11-67. Leicester University Press,
627 Leicester.
628 EPICA Community Members, 2006. One-to-one coupling of glacial climate
629 variability in Greenland and Antarctica. Nature 444, 195-198.
630 Fleitmann, D., Burns, S.J., Mudelsee, M., Neff, U., Kramers, J., Mangini, A., Matter,
631 A. 2003. Holocene Forcing of the Indian Monsoon Recorded in a Stalagmite from
632 Southern Oman. Science. 300, 1737-1739.
633 Folk, R.L., Ward, W.C., 1957. Brazos River bar: a study in the significance of grain-
634 size parameters. J. Sediment. Petrol. 27, 3-26.
635 Frierson, D.M.W., Hwang, Y.T., Fuckar, N.S., Seager, R., Kang, S.M., Donohoe, A.,
636 Maroon, E.A., Liu, X.J., Battisti, D.S., 2013. Contribution of ocean overturning
637 circulation to tropical rainfall peak in the Northern Hemisphere. Nature Geosci. 6,
638 940-944.
639 Gent, P.R., 2016. Effects of Southern Hemisphere wind changes on the meridional
640 overturning circulation in ocean models.Annu. Rev. Mar. Sci. 8, 79-94.
641 Ghil, M., Allen, R. M., Dettinger, M. D., Ide, K., Kondrashov, D., Mann, M. E.,
642 Robertson, A., Saunders, A., Tian, Y., Varadi, F., Yiou, P., 2002. Advanced
643 spectral methods for climatic time series, Reviews of Geophysics 40(1), 3.1-3.41,
644 10.1029/2000RG000092.
645 Govil, P. , Naidu, P.D., 2011. Variations of Indian monsoon precipitation during the
646 last 32 kyr reflected in the surface hydrography of the Western Bay of Bengal.

Quat. Sci. Rev. 30, 3871-3879.

Grootes, P.M., Stuiver, M., White, J.W.C., Johnsen, S., Jouzel, J., 1993. Comparison of oxygen isotope records from the GISP2 and GRIP Greenland ice cores. Nature. 366, 552-554.

Hammer, Ø., Harper, D. A. T., Ryan, P. D., 2001. Past: paleontological statistics software package for education and data analysis. Palaeontologia Electronica 4(1), art. 4: 9pp., 178kb.

Hemming, S. R., 2004. Heinrich events: Massive late Pleistocene detritus layers of the North Atlantic and their global climate imprint. Reviews of Geophysics 42, RG1005, doi:10.1029/2003RG000128

Hong, Y.T., Hong, B., Lin, Q.H., Yasuyuki, S., Hirotab, M., Zhu, Y.T., Leng, X.T., Wang, Y., Wang, H., Yi, L., 2005. Inverse phase oscillations between the East Asian and Indian Ocean summer monsoons during the last 12000 years and paleo-El Nin~o. Earth Planet. Sci. Lett. 231, 337-346.

Hu, S. Y., Goddu, S.R., Herb, C., Appel, E., Gleixner, G., Wang, S.M., Yang, X. D., Zhu, X.H., 2015. Climate variability and its magnetic response recorded in a lacustrine sequence in Heqing basin at the SE Tibetan Plateau since 900 kyr. Geophys. J. Int. 201, 444-458.

Hu, S.Y., Goddu, S.R., Appel, E., Verosub, K., 2007. Fine-tuning of age integrating magnetostratigraphy, radiocarbon dating and carbonate cyclicity: example of lacustrine sediments from Heqing basin (Yunnan, China) covering the past 1 Myr, J. Asian Earth Sci. 30, 423-432.

Hu, S.Y., Goddu, S.R., Appel, E., Verosub, K., Yang, X.D., Wang, S.M., 2005. Palaeoclimatic changes over past one million years derived from lacustrine Sediments of Heqing Basin (Yunnan, China), Quatern. Int. 136, 123-129.

Huang, C., Wei, G.J., Ma, J.L., Liu, Y., 2016. Evolution of the Indian summer

673 monsoon during the interval 32.7–11.4 cal. kyr BP: Evidence from the Baoxiu
674 peat, Yunnan, southwest China. J. Asian Ear. Sci. 131,72-80.
675 Jiang, X.Y., He, Y.Q., Shen, C.C., Lee, S.Y., Yang, B., Lin, K., Li, Z.Z., 2014.
676 Decoupling of the East Asian summer monsoon and Indian summer monsoon
677 between 20 and 17 kyr. Quat. Res. 82, 146-153.
678 Jiang, Z.X. and Liu Q.S., 2016. Quantification of hematite and its climatic
679 significances. Quat. Sci. 36, 676-689. (in Chinese)
680 Jo, K.N., Woo, K.S., Yi, S., Yang, D.Y., Lim, H.S., Wang, Y.J., Cheng, H., Edwards,
681 R.L., 2014. Mid-latitude interhemispheric hydrologic seesaw over the past 550,000
682 years. Nature 508, 378-382.
683 Jouzel, J. et al, 2007. Orbital and millennial Antarctic climate variability over the past
684 800,000 years. Science 317, 793 – 796.
685 Kalnay, E., Kanamitsu, M., Kistler, R., Collins, W., Deaven, D., Gandin, L., Iredell,
686 M., Saha, S., White, G., Woollen, J., Zhu, Y., Chelliah, M., Ebisuzaki, W.,
687 Higgins, W., Janowiak, J., Mo, K.C., Ropelewski, C., Wang, J., Leetmaa, A.,
688 Reynolds, R., Jenne, R., Joseph, D., 1996. The NCEP/NCAR 40-year reanalysis
689 project. Bull. Am. Meteorol. Soc. 77, 437-471.
690 King, J.W., Channell, J.E.T., 1991. Sedimentary magnetism, environmental
691 magnetism, and magnetostratigraphy. Rev. Geophys. 29, 358-370.
692 Knutti, R., Fluckiger, J., Stocker, T.F., Timmermann, A., 2004. Strong hemi-spheric
693 coupling of glacial climate through freshwater discharge and ocean circulation.
694 Nature. 430, 851-856.

695 Kornfeld, D., Sonntag, B.L., Gast, S., Matthes, J., Ratschbacher, L., Pfänder, J.A.,
696 Eckert, S., Liu, D.L., Appel, E., Ding, L., 2014. Apparent paleomagnetic rotations
697 reveal Pliocene-Holocene internal deformation of the Tengchong Block,
698 southeastern Tibetan Plateau. J. Asian Ear. Sci. 96, 1-16.
699 Laskar, J., Robutel, P., Joutel, F., Gastineau, M., Correia, A.C.M., Levrard, B., 2004.
700 A long term numerical solution for the insolation quantities of the Earth. Astron.
701 Astrophys. Manuscr. 428, 261-285.
702 Li, D.M., Li, Q., Chen, W.J., 2000. Volcanic activities in the Tengchong volcano area
703 since Pliocene. Acta Petrologica Sinica. 16, 362-370. (in Chinese)
704 Li, H, Y,, Zhang, H. C., Chen, G. J., Chang, F. Q., Duan, L. Z., Wang, J. Y., Lu, H.
705 B., Wu, H., Hu, K., 2017. The Grain Size Distribution Characteristics of Surface
706 Sediments from Plateau Lakes in Yunnan Province and Their Environmental
707 Significances. Acta Sedimentologica Sinica 35(3), 499-507 (in Chinese)
708 Liu, J.Q., Lu, H.Y., Negendank, J., Mingram, J., Luo, X.J., 2000. Periodicity of
709 Holocene climatic variations in the Huguangyan Maar Lake. Chin. Sci. Bull. 45,
710 1712-1717.
711 Liu, S.Z., Deng, C.L., Xiao, j., Li, J.H., Paterson G.A., Chang, L., Yi, L., Qin, H.f.,
712 Zhu, R.X., 2016. High-resolution enviromagnetic records of the last deglaciation
713 from Dali Lake, Inner Mongolia. Palaeogeogr. Palaeocl. Palaeoecol. 454, 1-11.
714 Maher, B. A., 1988, Magnetic properties of some synthetic sub-micron magnetites,
715 Geophys. J., 94, 83-96.
716 Marshall, J., Donohoe, A., Ferreira, M., McGee, D., 2014.The ocean's role in setting
717 the mean position of the Inter-Tropical Convergence Zone. Clim. Dyn. 42, 1967-
718 1979.

719 Marzocchi, A., Jansen, M.F., 2017. Connecting Antarctic sea ice to deep-ocean
720 circulation in modern and glacial climate simulations. Geophys.Res. Lett., 44,
721 6286-6295.
722 Mcgee, D., Donohoe, A., Marshall, J., Ferreira, D., 2014. Changes in ITCZ location
723 and cross-equatorial heat transport at the Last Glacial Maximum, Heinrich Stadial
724 1, and the mid-Holocene. Earth Planet. Sci. Lett. 390, 69-79.
725 Nesbitt, H.W., Young, G.M., 1982. Early Proterozoic climates and plate motions
726 inferred from major element chemistry of lutites. Nature. 299, 715-717.
727 Nowaczyk, N.R., Minyuk, P., Melles, M., Brigham-Grette, J., Glushkova, O., Nolan,
728 M., Lozhkin, A.V., Stetsenko, T.V., Andersen, P.M., Forman, S.L., 2002.
729 Magnetostratigraphic results from impact crater Lake El'gygytgyn, northeastern
730 Siberia: a 300 kyr long highresolution terrestrial palaeoclimatic record from the
731 Arctic. Geophys. J. Int. 150, 109-126.
732 Pedro, J.B., Ommen, T.D.V., Rasmussen, S.O., Morgan, V.I., 2011. The last
733 deglaciation: timing the bipolar seesaw. Clim. Past. 7, 671-683.
734 Qin, X. G., Cai, B. G, Liu, T. S., 2005. Loess record of the aerodynamic environment
735 in the east Asia monsoon area since 60,000 years before present. Journal of
736 Geophysical Research 110, B01204, doi:10.1029/2004JB003131.
737 Rashid, H., England, E., Thompson, L., Polyak, L., 2011. Late Glacial to Holocene
738 Indian Summer Monsoon Variability Based upon Sediment Records Taken from
739 the Bay of Bengal. Terr. Atmos. Ocean. Sci. 22, 215-228.
740 Rawat, S., Gupta, A.K., Srivastava, P., Sangode, S.J., Nainwal, H.C., 2015. A 13000

741 year record of environmental magnetic variations in the lake. Palaeogeogr.
742 Palaeocl. Palaeoecol. 440, 116-127.
743 Reimer, P. J., Baillie, M.G.L., Bard, E., Bayliss, A ., Beck, J. W., Blackwell, P.G.,
744 Ramsey, C.B., Buck, C.E., Burr, G.S., Edwards, R.L., Friedrich, M., Grootes, P.M,
745 Guilderson, T.P., Heaton, T.J., Hogg, A.G., Hughen, K.A., Kaiser, K.F., Kromer,
746 B., McCormac, F.B., Manning, S.W., Reimer, R.W., Richards, D.A., Southon,
747 J.R., Talamo, S., Turney, C.S.M., Plicht, J., Weyhenmeyer, C.E., 2009. IntCal09
748 and Marine09 radiocarbon age calibration curves, 0-50,000 years cal BP.
749 Radiocarbon. 51, 11-50.
750 Rosales, L.A.C., Jennerjahn, T., Tharammal, T., Meyer, V., Lückge, A., Paul, A.,
751 Schefuß, E., 2014. Evolution of the Indian Summer Monsoon and terrestrial
752 vegetation in the Bengal region during the past 18 kyr. Quat. Sci. Rev. 102, 133-
753 148.
754 Schulz, H., Rad, U.V., Erlenkeuser, H., 1988. Correlation between Arabian Sea and
755 Greenland climate oscillations of the past 110,000 years. Nature. 393, 54-57.
756 Sun, Q.L., Wang, S.M., Zhou, J., Chen, Z.Y., Shen, J., Xie, X.P., Wu, F., Chen, P.,
757 2010. Sediment geochemistry of Lake Daihai, north-central China: implications for
758 catchment weathering and climate change during the Holocene, J. Paleolimnol. 43,
759 75-87.
760 Thompson, R. and Oldfield, F., 1986. Environmental Magnetism. Allen and Unwin,
761 London.

762 Vellinga, M. and Wood, R.A., 2002. Global climatic impacts of a collapse of the
763 Atlantic Thermohaline circulation. Cli. Dym. 54, 251-267.
764 WAIS Divide Project Members, 2015. Precise interpolar phasing of abrupt climate
765 change during the last ice age. Nature 520, 661 – 664.
766 Wang, Q., Yang, X.D., Anderson, J.N., Zhang, E.L., Li, Y.L., 2014. Diatom response
767 to climate forcing of a deep, alpine lake (Lugu Hu,Yunnan, SW China) during the
768 Last Glacial Maximum and its implications for understanding regional monsoon
769 variability. Quat. Sci. Rev. 86, 1-12.
770 Wang, Q., Yang,X.D., Anderson, N.J., Zhang, E.L., Li, Y.L., 2014. Diatom response
771 to climate forcing of a deep, alpine lake (Lugu Hu, Yunnan, SW China) during the
772 Last Glacial Maximum and its implications for understanding regional monsoon
773 variability. Quat. Sci. Rev. 86, 1-12.
774 Wang, X.F., Auler, A.S., Edwards, R.L., Cheng, H., Cristalli, P.S., Smart, P.L.,
775 Richards, D.A., Shen, C.C., 2004. Wet periods in northeastern Brazil over the past
776 210 kyr linked to distant climate anomalies. Nature. 432, 740-743.
777 Wang, Y.F., Zhu, Y.X., Pan, H.X., Yin, Y., 2002. Environmental characteristics of an
778 acid Qinghai Lake in Tengchong, Yunnan Province. J. Lake Sci. 14, 117-124. (In
779 Chinese)
780 Wang, Y.J., Cheng, H., Edwards, R.L., He, Y., Kong, X., An, Z.S., Wu, J.Y., Kelly,
781 M.J., Dykoski, C.A., Li, X., 2005. The Holocene Asian monsoon: links to solar
782 changes and North Atlantic climate. Science 308, 854-857.
783 Weber, M.E., Clark, P.U., Kuhn, G., Timmermann, A., Sprenk, D., Gladstone, R.,

784 Zhang, X., Lohmann, G., Menviel, L., Chikamoto, M.O., Friedrich, T., Ohlwein,
785 C., 2014. Millennial-scale variability in Antarctic ice-sheet discharge during the
786 last deglaciation. Nature 510, 134-138.
787 White, A.F. and Blum A.E., 1995. Effects of climate on chemical weathering in
788 watersheds. Geochim. Cosmochim. Acta. 59, 1729-1747.
789 Wu, D., Zhou, A.F., Chen, X.M., Yu, J.Q., Zhang, J.W., Sun, H.L., 2015.
790 Hydrological and ecosystem response to abrupt changes in the Indian monsoon
791 during the last glacial, as recorded by sediments from Xingyun Lake, Yunnan,
792 China. Palaeogeogr. Palaeocl. Palaeoecol. 421, 15-23.
793 Xiao, X.Y., Shen, J.I., Haberle, S.G., Han, Y., Xue, B., Zhang, E.L., Wang, S.M.,
794 Tong, G.B., 2015. Vegetation, fire, and climate history during the last 18 500 cal a
795 BP in south-western Yunnan Province, China. J. Quat. Sci. 30, 859-869.
796 Xu, H., Zhou, X.Y., Lan, J.H., Liu, B., Sheng, E.G., Yu, K.K., Cheng, P., Wu, F.,
797 Hong, B., Yeager, K.M., Xu, S., 2015. Late Holocene Indian summer monsoon
798 variations recorded at Lake Erhai, Southwestern China. Quat. Res. 83, 307-314.
799 Xue, F., Wang, H.J., He, J.H., 2004. Interannual variability of Mascarene high and
800 Australian high and their influences on East Asian summer monsoon. J.
801 Meteorologi. Soc. Jap. 82, 1173-1186.
802 Yancheva, G., Nowaczyk, N.R., Mingram, J., Dulski, P., Schettler, G., Negendank,
803 J.F.W., Liu, J.Q., Sigman, D.M., Peterson, L.C., Haug, G.H., 2007. Influence of
804 the intertropical convergence zone on the East Asian monsoon. Nature 445, 74-77.

Yang, Y.P., Zhang, H.C., Chang, F.Q., Meng, H.W., Pan, A.D., Zheng, Z., Xiang, R., 2016. Vegetation and climate history inferred from a Qinghai Crater Lake pollen record from Tengchong, southwestern China. Palaeogeogr. Palaeocl. Palaeoecol. 461, 1-11.

Zhang, E.L., Sun, W.W., Zhao, C., Wang, Y.B., Xue, B., Shen, J., 2015. Linkages between climate, fire and vegetation in southwest China during the last 18.5 ka based on a sedimentary record of black carbon and its isotopic composition. Palaeogeogr. Palaeocl. Palaeoecol. 435, 86-94.

Zhang, E.L., Zhao, C., Xue, B., Liu, Z.H., Yu, Z.C., Chen, R., Shen, J., 2017. Millennial-scale hydroclimate variations in southwest China linked to tropical Indian Ocean since the Last Glacial Maximum. Geology 45 (5), G38309.1.

Zhang, J. W., Chen, F. H., Holmes, J. A., Li, H., Guo, X. Y., Wang, J. L., Li S., Lu Y.B., Zhao, Y, Qiang, M. R., 2011. Holocene monsoon climate documented by oxygen and carbon isotopes from lake sediments and peat bogs in China: a review and synthesis. Quat. Sci. Rev. 30, 1973-1987.

Zhao, K., Wang, Y.J., Edwards, R.L., Cheng, H., Liu, D.B., 2010. High-resolution stalagmite δ18O records of Asian monsoon changes in central and southern China spanning the MIS 3/2 transition. Earth Planet. Sci. Lett. 298, 191-198.

Zhu, X.Y., Zhang, M.L., Cheng, H., Wu, X., Edwards, R.L., 2015. Centennial- scale monsoon climate fluctuations from a stalagmite record during the mid-Holocene epoch in Fulu cave of Huaping,Yunnan, China. Environ. Earth. Sci. 74, 929-935.

826

Highlights:

- A reliable Indian Summer Monsoon (ISM) record during 35-1 ka is reconstructed from lacustrine sediment.
- Regional comparison corroborates the stage variations of lake level and weathering process.
- Multi-periods and components of ISM proxies suggest the competing influence of Southern and Northern Hemisphere.

Indian Summer Monsoon variations and competing influences between hemispheres since ~35 ka recorded in Tengchongqinghai Lake, southwestern China

Jie Peng[1], Xiaoqiang Yang[1]*, Jaime L Toney[2]*, Jiaoyang Ruan[1], Guanhua Li[1], Qixian Zhou[1], Huahong Gao[1], Yixuan Xie[1], Qiong Chen[1], Tingwei Zhang[1]

School of Earth Science and Engineering/Guangdong Provincial Key Laboratory of Geodynamics and Geohazards, Sun Yat-sen University, Guangzhou, 510275, China;

2. Geographical & Earth Sciences, University of Glasgow, +44 (0)141 330 6864, UK

E-mail: eesyxq@mail.sysu.edu.cn

Abstract

The southwestern Yunnan Province of China, which is located at the southeastern margin of the Tibetan Plateau and close to Bay of Bengal, is significantly influenced by the Indian Summer Monsoon (ISM). In this study, we reconstruct proxies for the ISM from 35 to 1 ka through detailed analysis of grain-size distribution, geochemical composition and environmental magnetism from a 7.96 m sediment core from Tengchongqinghai Lake, Yunnan Province, China. Globally recognized, abrupt climatic events, including Heinrich Events 0-3 (H0-H3) and the Bølling-Allerød (B/A) warm period are identified in most of our proxies, and the long-term trend is consistent with other published records such as stalagmite oxygen isotopes ($\delta^{18}O$) from Sangxing Cave. Northern Hemisphere (NH) temperature, which

is influenced by NH solar insolation, is commonly suggested to play a dominant role in controlling the ISM. A comparison of our record with the $\delta^{18}O$ variations of ice cores from Greenland and Antarctica, a sea surface temperature (SST) record from the Bay of Bengal, and summer solar insolation at 25^{o}N latitude demonstrates that the general pattern of ISM change does follow variations in summer insolation; however, the ISM lags summer insolation by thousands of years. While the ISM fluctuations are highly correlated with NH temperature on shorter timescales (centennial-millennial), the gradually weakened ISM from 22.5 ka until the Last Glacial Maximum（LGM) indicates a close relationship with the rise of Southern Hemisphere (SH) temperature and the relatively cold background of the SH. Our record expands on the findings of ISM records from Heqing paleolake basin in southwestern China and the Arabian Sea sediments, suggesting that the NH and SH have a competitive influence on ISM by controlling the cross-equatorial pressure gradient. This relationship means that when NH temperatures are relatively high, it has a stronger influence on the ISM than SH influences. In contrast, when the SH temperature is relatively low, it has a dominant influence on ISM. In addition, we speculate that the change of SH temperature not only influences the cross-equatorial pressure gradient directly, but also likely modulates the circulation system of ocean energy by influencing the Atlantic Meridional Overturning Circulation (AMOC).

Key Words: Lacustrine sediment; Indian Monsoon; Lake level; Chemical weathering; Southern Hemisphere.

1. Introduction

The Indian summer monsoon (ISM) is one of major component of the Asian monsoon system, it responds to the hydrology and energy circulation of the coupled atmosphere–ocean–land system and in turn plays a significant role in the global climate (Clemens, 1988; An et al., 2011; Caley et al., 2013; Rosales et al., 2014). Numerous high-resolution paleoclimatic records from natural lacustrine and oceanic sediments and cave deposits have revealed the origin, forcing mechanism and evolution of the ISM over the last 20 years (Fleitmann et al., 2003; Clemens and Prell, 2003; Zhang et al., 2004; Hu et al., 2005, 2007, 2015; An et al., 2011; Deplazes et al., 2013; Rosales et al., 2014; Xiao et al., 2014; Chen et al., 2014; Wang et al., 2015; Wu et al., 2015; Xu et al., 2015; Zhang et al., 2015, 2017). These records suggest that on the glacial-interglacial time-scales, solar insolation of the NH has played the dominant role in the ISM development by controlling the NH temperature (Clemens et al., 2003; Deplazes et al., 2013; Wang et al., 2014; Xiao et al., 2015). In addition, SH temperature has also been suggested to influence monsoon variability by controlling the high-pressure source of the cross-equatorial pressure gradient system in the glacial period, but evidence for this remains scarce (An et al, 2011; Caley et al., 2013). On millennial and centennial time-scales, North Atlantic cold events are implicated in abrupt ISM variations by influencing the AMOC, which has global ocean-air energy links and could affect the location of ITCZ (Alley et al., 1997; Clemens et al., 2003; Hong et al., 2005; Dah et al., 2005; Yancheva et al., 2007; Ziegler et al., 2010; Deplazes et al., 2013). The influence of the SH on millennial time-scales, however, is not well-studied. Interhemispheric temperature and precipitation, especially in the period of global climate fluctuations (such as Heinrich events and Dansgaard-

Oeschger (D-O) events) show an inverse relationship between the NH and SH (Blunier and Brook, 2001; Barker et al., 2009; Pedro et al., 2011; Jo et al., 2014), which is called the "bipolar see-saw" pattern (Blunier, et al., 2001). These phenomena mean that SH climate also influences the ISM by regulating the teleconnections of the global ocean and atmosphere circulation system (Xue et al., 2004; Chiang et al., 2005; Anderson et al., 2009; Gent 2016; Marzocchi and Jansen, 2017). However, the specific influence mechanism needs to be clarified further by additional ISM archives.

Southwestern China, located to the southeast of the Himalayan Mountains, is the key region of the ISM influence of China. The temperature and precipitation of this area are strongly affected by the dynamics of the ISM (An et al., 2011; Chen et al., 2014; Cai et al., 2015; Xiao et al., 2015). Previous paleoclimatic reconstructions of this region using lacustrine sediments and stalagmites showed that the ISM has experienced different stages since the late Pleistocene (Zhang et al., 2011; Xiao et al., 2014; Chen et al., 2014; Wang et al., 2015; Wu et al., 2015; Xu et al., 2015; Zhang et al., 2015, 2017). In addition, the globally recognized periods, such as, the Last Glacial Maximum (LGM) and abrupt millennial or centennial scale climatic fluctuations, such as the Bølling-Allerød interstadial (B/A), Heinrich events (H1-H4) have been identified (Xiao et al., 2014; Chen et al., 2014; Wang et al., 2015; Wu et al., 2015; Xu et al., 2015; Zhang et al., 2015, 2017).

Because most of these previous studies cover relatively short time periods, long, continuous records from appropriate geographical regions are needed to comprehensively understand controls and processes specific to the ISM. Moreover, the combination of multiple climate proxies will help solve the limitations of interpretations based on single proxies (Deplazes et al., 2013; Calay et al., 2013). Two previous studies have reconstructed paleo-fire history and ecosystem hydroclimate

variations of southwestern China from Tengchongqinghai Lake (TCQH) over the past 18 ka and 15.8 ka, respectively (Xiao et al., 2015; Zhang et al., 2015, 2017; Yang et al., 2016). These studies indicate that TCQH sediments are the ideal archive for ISM study, because it has a stable catchment and is uniquely sensitive to ISM variability. Therefore, a longer sediment core, QH4, was drilled in 2014. Here, we present the high-resolution paleoclimate study of QH4 based on grain-size distribution, major geochemical composition, and environmental magnetism over circa the last 35 cal ka BP. This exceptionally long and continuous record allows for the reconstruction of the ISM evolutionary history and determine the competing NH and SH forcing mechanisms related to the ISM.

2. Regional setting

Lake TCQH (25°08′06″-25°07′44″N, 98°34′11″-98°34′26″E; elevation ca. 1850 m) is situated in Tengchong County, Yunnan province, southwestern China (Fig. 1). It is a crater lake with a surface area is about 0.25 km^2. The average water depth is 5.2 m while the maximum water depth was 8.2 m in 2013; The lake is surrounded by hills with the relative altitudes of 120-200 m and 60-140 m on the east and west sides, respectively. In the south-east direction, the gently increased terrain provides the most of deposition detritus. There isn't any external river which brings stable input, the sediments all come from the surrounding small hills and the total catchment area is only about 1.5 km^2. As a result, the lake is sensitive to the hydroclimate of this region. The bed-rocks in the catchment consist of andesite, basalt and tuffaceous breccia. The top soil is about 1-2 m in thickness covered with plenty of vegetation.

Located at the southeastern edge of the Tibetan Plateau and western Gaoligongshan Mountain (Wang et al., 2002), the moist wind from the Arabian Sea

and Bay of Mengal could bring abundant rainfall to fed the lake in summer just as the modern atmospheric observations indicated as Fig. 1 shows. However, the winter monsoon less affects the lake as the blocking of Gaoligongshan Mountain. The annual average temperature is about 15.9℃ and annual precipitation is about 1492 mm. As Fig. 2 shows, Tengchong actually has a typical monsoon climate, about 75% of precipitation is supplied between May and September. Therefore, the sedimentation of TCQH could reliably record the evolution history of the ISM.

3. Material and methods

3.1. Sampling

In 2014, a 16.96 m long sediment core, QH4 (25°7.871' N, 98°34.388' E), was drilled to the bed rock in a water depth of 2.13 m using a gravity piston corer in northeast of TCQH basin. In this paper, we focus on the depth interval of 0.21-7.96 m in the core. We chose this interval because the upper 0.21 m section was disturbed by fishing activities and the section below 7.96 m lacks chronological references for dating. The sediments of core composed mainly of grey-black clayey silt with the variant color in the different layer. Following is a brief introduction to the section from the top to the bottom:

a. 0-3 m, Dark grey clayey silt with rich organic content;

b. 3-3.8 m, Gray-black clayey coarse silt dotted with fine sand;

c. 3.8- 5.24 m, Dark gray to light brown clayed silt dotted with a little of gray-green volcanic ash spots;

d. 5.24-5.68 m, Colorful volcanic ash deposits or rapid runoff sediments comprising of silt, fine sand and small gravel with less organic content;

e. 5.68-6.06 m, Dark silty clay with high organic content;

f. 6.06-6.65 m, Light brown yellow silty clay;

g. 6.65-7.96 m, Light gray-black silty clay stained with a little of offwhite or light blue ash spots.

One half was continuously sampled by pushing plastic cubes ($2\times2\times2$ cm^3) into the split face of the core sections for environmental magnetism analysis, and a total of 276 samples were obtained. The remaining half was also sliced continuously at 2 cm intervals. and the samples were freeze-dried for the other analyses.

3.2. Methods

The chronology of the core was established with accelerator mass spectrometer radiocarbon ^{14}C (AMS ^{14}C) dating of nine plant remains (tree branches or leaves) and four bulk sediment samples, which were analyzed at Beta Analytic Testing Laboratory, USA. The conventional AMS ^{14}C ages were calibrated using the $CALIB_{702}$ program (IntCal13 data set, Reimer et al., 2009). The age-depth model was established using Bacon software (Blaauw and Christen, 2011). Grain-size analysis of all samples was performed using a Malvern Instruments Mastersizer-3000 at Sun Yat-Sen University for all sample. Prior to measurement, organic matter and carbonate were removed using 10% H_2O_2 and HCl, respectively. The grain size data was analyzed using Malvern software and following the methods suggested by Simon et al (2001) and Qin et al. (2005) respectively at last. Geochemical major elemental concentrations were measured at 8 cm interval using an X-ray fluorescence spectrometer (XRF, Rigaku ZSX Primus-Ⅱ) at Sun Yat-Sen University. The carbonate content was removed using 10% HCl. Then the samples were hand-milled

by the agate mortar and prepared for analysis after sieving through a 250 mm sieve. Firstly, the sample was ignited in muffle furnace for 2 h at 900 ℃. Then the baked sample was fused with a 2:1 mix of lithium tetraborate and lithium metaborate, at 1050 ℃ for 20 minutes, to form a glass bead for test. The chemical weathering index CIA is defined as $Al_2O_3/(Al_2O_3 + CaO^* + Na_2O + K_2O)\times100$, where CaO* indicates the calcium content in the silicate fraction of the sediments (Nesbitt and Young, 1982). Magnetic susceptibility-Temperature measurements (χ-T curves) for representative four samples were measured in the Institute of Geology and Geophysics, Chinese Academy of Sciences. Analysis was performed in an argon atmosphere using an AGICO MFK1-FA equipped with CS-3 temperature control system and with temperature ranging from 25℃ to 700℃ with a ramping rate of 2℃/min in this study. Environmental magnetic measurements for the all samples were performed on the 276 samples in the Institute of Geology and Geophysics, Chinese Academy of Sciences. The low-field magnetic susceptibility (κ) was measured using a Bartington MS2 meter with the frequency at 470 Hz. Isothermal remanent magnetization (IRM) was induced with direct current (DC) fields of 1T and -300 mT with a 2G Enterprises model 660 pulse magnetizer, the saturation IRM (SIRM) and IRM_{-300mT} were measured using a 2G-760 IRM system. S-ratio is defined as the ratio of IRM_{-300mT} to SIRM (King and Channell, 1991) for estimating the relative contributions of low-coercivity magnetic minerals, with the "hard" fraction of IRM (HIRM) defined as 0.5 $\times$ (IRM_{1T} + $IRM_{-300\ mT}$) (Thompson and Oldfield, 1986), which is oppositely indicated by the absolute concentration of high-coercivity magnetic minerals. Anhysteretic remanent magnetization (ARM) was produced in an alternating field of 80 mT peak field superimposed over a 0.05 mT DC field using a 2G-760 ARM system. Ten typical samples with high coercivity based on the HIRM data were chosen for

188 measurement of the diffuse reflectance spectrophotometry (DRS) (Deaton and Balsam,
189 1991) using the Perkin Elmer spectrophotometer in Sun Yat-Sen University. The
190 selected samples were evenly coated on the glass with the distilled water and scanned
191 from 400 to 700 nm in 0.50 nm steps after being dry naturally.

192 # 4. Results

193 ## 4.1. AMS ^{14}C dating result

194 As shown in Table 1, the age of the bottom sediments is 35.08 ± 0.38 cal ka B.P.
195 and the average sediment accumulation rate is about 4.5 ka/m. There is one specific
196 abnormal, non-laminated section from 5.24 m to 5.73 m, where the dominant
197 composition is gray tufa masses of irregular grain-size. We speculate that it might
198 have been washed into the lake abruptly or come from a volcanic eruption within a
199 short time, so we take the average value of all the proxies of the 49 cm section as one
200 representative sample, which avoids misrepresentation of the sediment rate and time-
201 depth relationship.

202 ## 4.2. Grain-size and geochemical major elements results

203 Generally, grain size distributions of samples display unimodal or bimodal
204 (Suppl. 1), poorly sorted. The mean grain size (using the FOLK and WARD method
205 (Blott & Pye, 2001)) varied around 9.04 μm (std.=3.77) , the skewness and kurtossis
206 were characterized with the mean values -0.055 (std.=0.071) and 0.998 (std.=0.065),
207 respectively. The bimodal and little positive skewness just mainly occurred between
208 the 29-33 ka, corresponding to the larger sorting values. The fraction of very fine silt
209 and clay (<4 μm) contributes the component of about 27.3%. Three independent

components can be separated for all samples (Qin et al., 2005). The size of the first component is generally less than 1.3 μm, and the second predominant component distributed within the size of 1.3-63 μm with varied median grain size from 5 μm to 15 μm; the size of the third component is mainly between 63 and 1000 μm. The grain fraction of <1.3 μm, 1.3-5 μm (FGS) and 1.3-15 μm show an agreement pattern, which is opposite to the variations 63-1000 μm (Figure 4). A series of climate events, such as cold events H0-H3 and warm event B/A can be recognized by low FGS fraction and relative high coarse fraction (Hemming & Sidney, 2004). The proportion of grain size from 1.3 to 5.0 μm (FGS), the gradually increased part possessing a mean fraction 29% in the second component defined by two inflexion, which is more sense to the relative level fluctuations, roughly relating to the less sorting values. The grain size distribution along with the time scale can be divided into five stages:

First stage (a, 35-29 ka), FGS varied from a high content to relative low, corresponding the coarse grain fraction increase rapidly, which may arise from the contributions of volcanic detritus influx. The second stage (b, 29-19.2 ka) displays a gradually decreasing trend, and third stage (c, 19.2-15 kyr) possesses of the lowest vale, linking to the LGM period. The consequent fourth (d, 15-6.2 kyr) and fifth (e, 6.2-1 kyr) stages have again increased and then reduced fine fraction. Every stages are all punctuated with several significant narrow low vales and high peaks, presenting some rapid events.

The XRF results show the variations very similar to the fine grain size fraction (Figure 5). The high contents of TiO_2, Al_2O_3 and the ratio of Fe_2O_3/CaO_2, TiO_2/CaO_2 as well as the CIA index are close related to the high FGS fraction, and vice vesa. However, the sampling resolution are less than the particle analysis, thus missing some climate events information.

4.3. Rock magnetic and environment magnetic results

The κ-T curves of the typical samples substantially decrease during the 550-600 ℃ portion of the heating process, which demonstrates the thermal unblocking of major magnetic mineral-magnetite, as shown in Figure 6. There is a slightly decreasing trend after 600℃ as well, which usually indicates the presence of hematite. The obvious hump between 450 to 550 ℃ is probably the result of the neo-formation of magnetite transformed from iron-containing minerals such as silicates, clays or carbonates (Deng et al., 2001). The second derivative curves of DRF are shown in Figure 7, their characteristic bands center at about 450 nm and 580 nm, indicating goethite and hematite, respectively (Deaton and Balsam, 1991).

The volume susceptibility (κ) of most samples is relatively weak (with an average value of 2.2×10^{-5} SI) and all samples above the depth of 0.73 m are negative (close to zero, not shown), arising from the high organic content. The other concentration-dependent magnetic parameters, e.g. SIRM and ARM, have similar variations with the κ throughout the whole sequence.

S-ratio values of almost all samples are high (with an average value of 0.91), suggesting that values are controlled by the low-coercivity magnetic mineral magnetite. However, it is the high-coercivity magnetic mineral which give rise to the change of SIRM, κ and ARM throughout the whole sequence as HIRM being consistent with SIRM, κ and ARM, but not the S-ratio as shown in Figure 8.

5. Discussion

5.1. Environmental significance of the proxies

A series of investigation results present that the particle size in a closed lake can serve as a proxy indicating the lake level fluctuation (Qin et al., 2005; Zhang et al., 2017; Li et al., 2017). The proportion of fine grain (<16 μm) in the center of lake is clearly larger than that in the margin for the surface sediments (Zhang et al., 2017; Li et al., 2017). At the same site, the increasing fraction of fine grain along with the depth raised from rising lake level. TCQH lake is enclosed by small hills without other water system influx and outflow, and the deposition particles are mainly produced from the detrital materials by weathering base rock around the hills. Therefore, the grain-size can be viewed as an indicator of lake level, owning the grain-size of the sediments would progressively become smaller with the extended distance from the shoreline (Zhang et al., 2017). This is confirmed by previous detailed grain-size analysis of surface sediments from TCQH, where the small grain-size fraction (<16 μm; SGS) gradually increases from ~35% to ~65% with increasing lake water depths from ~2 m to ~6.5 m (Zhang et al., 2017). Therefore, the high percentage of SGS in certain site could indicates the periods of high lake level, and vice versa. As the nature rainfall controlled by the ISM consist of water source of TCQH lake, the gain-size change can also indicate the variation of the ISM strength indirectly.

As the hills surrounded the TCQH lake were formed by volcanic rock, the geochemical elements and magnetic minerals all come from the chemical weathering process. The weathering intense and the detritus influx are reasonably influenced by the precipitation (White & Blum, 1995). Enhanced effective precipitation and warm

climate would produce more plentiful detritus and transport to the lake. The well consistent between the contents of TiO_2, the ratio of Fe_2O_3/CaO and TiO_2/CaO, CIA index and magnetic proxies of SIRM, HIRM as well as the high fraction of fine grain, denote the commonly controlling factors. CIA is a well-established indicator of chemical weathering strength based on the fact that the major elements behave differently during the weathering processes (Nesbitt and Young, 1982). In addition, the ratios of major elements also have been widely used as the proxy of weathering (Sun et al., 2010; Engstrom and Wright, 1984). Following this principle, high TiO_2 and Al_2O_3 content, high ratios of TiO_2/CaO, Fe_2O_3/CaO and CIA indicate a strong ISM. The environmental magnetism parameters κ, ARM and SIRM are usually indications of magnetic mineral concentrations, and ARM is particularly sensitive to the stable single domain (SD) ferromagnetic particles (Maher, 1988; Hu et al., 2005). SIRM reflects the concentration of remanence carriers (ferromagnetic and antiferromagnetic particles). These proxies show strong correspondence throughout the core, suggesting that they are not greatly influenced by mineralogy and grain-size of the magnetic minerals (Liu et al., 2016). As the magnetic minerals originate from the weathering of exposed bedrock and surface soils in the catchment, their concentrations also reflect the weathering intensity and transporting capacity of runoff. DRF results indicate that goethite and hematite are the hard magnetism fraction of samples with high HIRM values. Commonly, iron oxidation requires an electrolyte, such as water (Davison and Seed 1983). Thus, the high HIRM correspond to a highly moisture environment with the strong ISM (Jiang et al., 2016; Hu et al., 2015). Besides, magnetic dissolution is ubiquitous in suboxic and anoxic environments (Liu et al., 2000; Duan et al., 2014). Thus, the high organic content would result in an environment supportive of dissolving magnetic minerals (especially SD ferrimagnetic

particles) (Nowaczyk et al., 2002; Duan et al., 2014), but enhanced oxygen concentration caused by wind could increase preservation of magnetic minerals, so strong ISM is benefit to both the production and preservation of magnetic minerals.

As illustration above, the fraction of fine grain suggests the lake level fluctuation, and chemical elements as well as its ratios accompanied with magnetic parameters influenced by the effective precipitation, weathering process and detritus influx. We processed the PCA analysis using CANO software for fine grain fraction， ARM/SIRM, SIRM, HIRM and the content of TiO_2, the results show that they are distributed in one quadrant, denoting the similar dominating climate factors. They can serve as the proxies of ISM.

5.2. Paleoclimate changes since the late last glacial period

Based on the signals from all paleoclimate proxies in this study, the period between 35-1 ka BP could be divided into 5 intervals (a-e) from bottom to top as shown in Fig. 4-5 and Fig. 8. Notably, there are significant ISM strength excursions during the periods of 32-29.8 ka BP, 15.8-15.2 ka BP, 14.7-14.2 ka BP, 8-7.5 ka BP, respectively.

In interval a (35-29 ka BP), the rich chemical elements, such as Al_2O_3, TiO_2, CIA and high magnetic assemblage indicate that the strong ISM enhanced the chemical weathering and resulted in more elements and magnetic minerals being transported into the lake. High fine grain fraction also indicates higher lake level. This is consistent with a sediment record in Xingyun Lake, which is 500 km away from TCQH. The highest percentages of pine forest and evergreen broadleaved forest

(dominated by evergreen *Quercus*) as well as the lowest percentages of mean grain-size both imply a relatively high lake level, which is the wettest period in the whole record from 36.4-13.4 ka BP (Chen et al., 2014; Wu et al., 2015). In addition, ISM strength declined significantly during the period of 31.95-29.8 ka BP, which might correspond to the global cold event Heinrich 3 (Broecker et al., 1992).

In interval b (29-19.2 ka BP), the elements, magnetic concentration and FGS content gradually decreased, showing a gradual weakening ISM trend.

In interval c (19.2-15 ka BP), this period can be recognized as the Last Glacial Maximum (LGM) characterized by the minimal major minerals, magnetic minerals and FGS since 35 ka BP.

In interval d (15-6.2 ka BP), the B/A warm event is shown by the remarkable increase of FGS fraction, SIRM and ARM. This event terminated the weakest ISM period (LGM) and began the strong ISM period until ~6.2 ka BP. During 7.8-8 ka BP, the Al_2O_3, TiO_2, SIRM show a slight fluctuation, which might correspond to the 8.2 ka cold event (Alley et al., 1997). However, the famous cold event YD is shown only in the grain-size below 16 μm.

In interval e (6.2-1 ka BP), the values of Al_2O_3, TiO_2, CIA, κ, ARM and SIRM are relatively low, indicating the weakening ISM since 6.2 cal ka BP. This is the popular milestone in Holocene climate change, which is also recorded in other ISM regions, such as the Bay of Bengal (turning at about 5 ka BP, Rashid et al., 2011) and Lahaul Himalaya (turning at about 5.77 ka BP, Rawat et al., 2015).

5.3. Comparison between regional climate history

The topography in Fig. 1 shows that the altitude along the path of the ISM (from

the Bay of Bengal to TCQH) is gradual increased, indicating that the ISM is a major climate driver in the TCQH catchment. To further confirm the reliability of our record, we compared them with the previous TCQH study results (Fig. 9B and Fig. 9C, Zhang et al., 2015, 2017) and other available records from the ISM region. In particular, records from southwestern China, such as stalagmite $\delta^{18}O$ from Xiaobailong Cave (Fig. 9A, Cai et al., 2015), geochemical minerals parameters K/Rb from Baoxiu peat (Fig. 9D, Huang et al., 2016), pollen percentage of cold tolerant conifers from Xingyun Lake (Fig. 9 E, Chen et al., 2014), stalagmite $\delta^{18}O$ from Sanxing Cave (Fig. 9F, Jiang et al., 2014) and Arabian Sea sediment reflectance L* (Fig. 9I, Deplazes et al., 2013) provide good comparators. As a whole, although the time span and resolutions of these records are not completely coincident, the overall trend and most distinct features are similar.

As Fig. 9 shows that the general trend of the stalagmite $\delta^{18}O$ record from Sanxing Cave is the most similar to SIRM of QH4 among the all regional records. The Sanxing $\delta^{18}O$ values increased from the most negative -8.1 ‰ to -6.0 ‰ gradually from 30.9 to 17 ka BP (Jiang et al., 2014), which is consistent with the decline in SIRM of TCQH. Although different climatic proxies were used and the distance between TCQH and Sanxing Cave is 500 km, they both shown the decreasing strength of the ISM from 30 to 17 ka BP. In conclusion, although there are differences in the latitude, elevation, distance to sea, topography and geomorphology of different ISM records, which have an inevitable impact on their climate (Clemens

et al., 2003), most of the records indicated the ISM was persistently decreasing during 30 to 17 ka BP.

5.4. Global correlations and the forcing of the ISM

Multiple lines of evidence indicate that NH temperature, controlled by the solar insolation, dominated the ISM evolution by influencing the migration of the ITCZ (Fleitmann et al., 2003, 2007; Deplazes et al., 2013; Xiao et al., 2014; Huang et al., 2016). Meanwhile, ISM events also correspond to North Atlantic ice rafted debris (IRD) events in most records (Schulz et al., 1988; Gupta et al., 2003; Ziegler et al., 2010; Deplazes et al., 2013). In addition, Zhang et al. (2017) suggests that the migration of ITCZ induced by solar insolation alone cannot account for the Holocene hydroclimate fluctuations of the eastern ISM domain. The large-magnitude fluctuations from 5 to 4 cal ka BP recorded by TiO_2 and grain-size in TCQH reveal the close links to the Arabian Sea sea-surface temperature (SST) and the ISM strength variations. Briefly, continental drainage could affect surface ocean conditions of the Andaman Sea and Bay of Bengal. In turn, slight increases in ocean SSTs might enhance moisture exchange from the ocean to the atmosphere and the enhanced moisture of atmosphere would then be transported to South Asia and southwestern China by the ISM. In other words, the ISM is subjected to complex influences from external and internal climate forcing, and in return, plays an important part in driving global air and energy systems (Caley et al., 2013; Rosales et al., 2014).

As we know, the ISM is formed from the cross-equatorial pressure gradient between the low atmosphere pressure (Indian low) over the Asian landmass and high pressure (Mascarene High) over the subtropical Indian Ocean (Clemens et al., 1998; Caley et al., 2013; Hong et al., 2005; An et al., 2011). Therefore, the lower the Indian

Low and/or the higher the Mascarene High, the stronger the intensity of the ISM. However, most previous studies of the ISM concentrate on changes in NH conditions that are influenced by only the Indian Low (Clemens et al., 2003; Wang et al., 2014; Xiao et al., 2015). One of major reasons for this is the lack of climate archives with high-resolution and dating certainties from the SH (Weber et al., 2014). In fact, even though NH temperature and large-scale climate events might dominate the ISM evolution, the influence coming from the SH is needed to further explore the "bipolar see-saw" connection between the climate of the NH and the SH (Blunier and Brook, 2001; Knutti et al., 2004; Jo et al., 2014). For example, the atmospheric methane records from the Greenland Ice Sheet Project 2 (GISP2) ice core and Antarctica Byrd ice core show that the onset of seven major millennial-scale warming events between 90 to 10 ka in Antarctica preceded the onset of Greenland warming events by 1.5 to 3 ka (Blunier and Brook, 2001). A stalagmite record from Korean Peninsula (in the NH) and Naracoorte, Southeastern Australia (in the SH) over the past ~550 ka also show an inter-hemispheric, hydrologic see-saw that extended to mid-latitudes from peak interglacial to mid-sized glacial periods (Jo et al., 2014). It is also generally accepted that climate variability in the NH is usually accompanied by temperature changes in Antarctica that is coupled through ocean thermohaline circulation (Knutti et al., 2004). We have sufficient evidence to infer that there must be a mechanistic link between the ISM and SH climate, which is related to the change of Mascarene High and/or Indian Low, either directly and/or indirectly.

We specifically compare our SIRM and FGS (grain-size 1.3-5 μm) records with the $\delta^{18}O$ record of the GRIP2 ice core from Greenland (Grootes et al., 1993), average summer insolation at 25°N (Laskar et al., 2004), the SST reconstruction from core SK218/1 collected from western Bay of Bengal (Govil and Naidu, 2011), and the $\delta^{18}O$

record from the ice core from European Project for Ice Coring in Antarctica (EPICA) in the Dronning Maud Land (EDML) (EPICA community members, 2006) (Fig. 10). We use these records below to supplement our new data and to explore the driving force (s) of the ISM since 35 cal ka BP by systematic and comprehensive analyses.

5.4.1. Long-term ISM evolution driven by summer insolation

Comparing proxies of QH4 with NH summer insolation indicates that the insolation provides the major forcing of ISM change, but there is an obvious lag of the ISM behind the insolation. We mainly focused on the weakest ISM of the QH4 record in about 15 ka. As Fig. 10 shows, the ISM change lags about 7 ka behind the weakest summer insolation at 25°N in 22 ka, just as the previous Arabian Sea sediment record indicated. It is shown that maximum summer surface water productivity of Arabian Sea lagged the precession-related maximum solar insolation by about 6 ka, which was suggested to be related to the cross-equatorial transport of latent heat (Reichart et al., 1998; Clemens et al., 2003).

5.4.2. Remarkable ISM fluctuations relate to bipolar temperature

Six strong millennial-to-centennial ISM peaks (a, b, c, d, e, f) occur in the QH4 SIRM and FGS curves and are consistent with the more positive $\delta^{18}O$ values of the GRIP2 ice core and the more negative $\delta^{18}O$ values of EDML ice core within the age uncertainties from 35-26 cal ka BP. The fluctuations of GRIP2 and QH4 records are remarkably sharper than EDML $\delta^{18}O$ record, while the SH temperature revealed relatively mild and cold conditions in this period. Based on these correlations, the ISM strong events are likely influenced by the temperature of the NH and SH together, but the NH played a leading role during this period. Notably, the increase of the SST

in the Arabian Sea from 30 to 26 cal ka BP did not strengthen the ISM.

5.4.3. ISM weakening influenced by SH temperature

The most outstanding feature of the ISM indicated by SIRM and FGS is the gradual weakened trend of ISM from 27 to 17.5 cal ka BP. However, what is worth noting is that this gradual weakening trend occurred, despite the fact that the NH temperature was rising from 22.5 to 19.2 ka. This means that the rising NH temperature did not strengthened the ISM intensity at this time. Surprisingly, SH temperature gradually increased from 27 to 14 ka, albeit more mildly before 18 ka. It appears that the SH exhibited a more important influence on the ISM by weakening the pressure gradient during this time. In addition, both NH and SH temperatures were relatively low throughout this time. The statistical test between Arabian Sea productivity records and bipolar climate records (NGRIP and EDML ice $\delta^{18}O$) in the interval of 40-16 ka also reveals a better correlation between Arabian Sea Br (a proxy for marine productivity) and EDML $\delta^{18}O$ records than NGRIP $\delta^{18}O$ records (Caley et al., 2013). Synthesizing the ISM record characteristics from 35 to 27 cal ka BP, we suggested that the SH does not play a significant role in controlling the ISM compared to the NH when the NH has relatively higher average temperatures. Whereas, the converse is true, that when the SH has lower temperatures, it has a stronger impact on the ISM than the NH. This rule is not only confirmed by the Arabian Sea Br records, but also is consistent with the Heqing Basin ISM proxies (weathering proxy (Rb/Sr) and biologic productivity proxy (TOC) at glacial-to-interglacial time-scales. Since 2.60 Ma, ISM minima occurred 14 to 35 ka earlier than the timing of NH glaciation maxima during the transition from interglacial into glacial. As a result, the ISM was slowly strengthening coeval with increasing NH glaciation, at the same time that SH

468 temperature was nearly at its lowest and Antarctic ice volume was increasing (An et
469 al., 2011). An et al. (2011) attribute the glacially strengthened ISM to the strong SH
470 atmospheric meridional circulation and intensified Mascarene High as a result of low
471 SH temperature and increased Antarctic ice volume. This pattern suggests that the
472 stage of cold temperatures in the SH is a required background state for influencing the
473 ISM. In fact, as Fig. 10 shows, after the B/A warm period, SH temperature remains
474 relatively high and showed no obvious control on ISM thereafter.

475 For the records of the $\delta^{18}O$ of ice core from EDML, EDC3 and GISP2 (Jouzel et
476 al., 2007; EPICA Community Members, 2006; WAIS Divide Project Members, 2015),
477 and the FGS fraction as well as ARM/SIRM, we further separate them into four
478 primary components (PC1-PC4) using the Singular Spectrum Analysis (SSA) method
479 and carry out the spectra analysis with PAST software respectively (Hammer et al.,
480 2001; Ghil et al, 2002) (Supp. 2). It is very clear that the periods ~3.8, ~1.5 and ~1.1
481 ka in grain fraction closely correspond to that those recorded in GISP2, while the
482 periods of ~4.0 ka and 2.5 ka in grain fraction and ARM/SIRM can only find the
483 counterpart in Antarctic records (Supp. 3). The almost consistent pattern of the FGS
484 and ARM/SIRM in the component 3 (PC3) illustrates the similar climate controlling
485 conditions. We compiled them into a synthesizing proxy after normalization, and
486 designated low proxy value as the weak ISM event. Thus, these events can be
487 numbered as 'Q1-Q14'. Almost all the weak ISM events related to the warm Antarctic
488 temperature except of events Q4 and Q6. Same results were proofed by the stalagmite
489 records in central China (Chen et al., 2016). We suppose that the influence of
490 Greenland climate to ISM should be connected by the global conveyor belt, which
491 transport the cold water to Indian Ocean, cooling the surface water and causing
492 weaken ISM; while Antarctic temperature adjust the atmospheric meridional

493 circulation rapidly.

494 5.4.4. How the SH temperature influences in ISM

495 Overall, there are two possible driving mechanisms of the ISM that are related to
496 SH temperature.

497 (1) Atmosphere modulation system

498 It is known that the ISM is controlled by the cross-equatorial pressure gradient,
499 mainly that the low pressure over Asia, which is caused by sensible heating of the
500 Asian land surface and latent heating derives from surface evaporation over Indian
501 Ocean (Clemens et al., 2003), and the high pressure, the Mascarene High, which is
502 closely related to the circumpolar low in high southern latitudes. Relatively low SH
503 temperature could induce great intensification of a high-pressure system over the
504 Mascarene region, and strengthen the cross-equatorial Somali jet as a result of ISM
505 being strengthened (Xue et al., 2004; Caley et al., 2013; Frierson et al., 2013).
506 Whereas, when the SH temperature increases, the ISM will correspondingly be
507 weakened.

508 (2) Ocean-atmosphere system

509 Another driving force for cross-equatorial pressure gradient comes from the
510 ocean-atmosphere circulation system. According to satellite observations and climate
511 model simulations, the Atlantic Meridional Overturning Circulation (AMOC) plays a
512 significant role in heat transport from SH to NH (Frierson et al., 2013). Previous
513 studies show that a massive supply of sea-ice and freshwater in North Atlantic Ocean
514 perturbed surface and deep waters of ocean (Alley et al., 1997; Bard et al., 2000),
515 which led to a change in the AMOC. This in turn influenced the position of ITCZ as
516 the close heat-cycle relationship exists between the AMOC and the ITCZ (Dahal et al.,

2005; Denton et al., 2010; Deplazes et al., 2013; Frierson et al., 2013; Marshall et al., 2014; McGee et al., 2014). In fact, more and more clues are offered by climate simulations and paleoclimate records support that the Antarctic sea ice and temperature could modulate the global climate change (Bintanja et al., 2013), especially by influencing the AMOC and atmospheric carbon dioxide concentrations (Vellinga and Wood, 2002; Barker et al., 2009; Marzocchi and Jansen, 2017).

6. Conclusions

Constrained by thirteen AMS ^{14}C ages, combined multi-proxies, such as geochemical properties (major elements concentration and CIA), geophysical parameters (environmental magnetism and rock magnetism) and lithological variations (grain-size) across the length of 7.76 m sediments core from TCQH, show the ISM evolution history in southwestern China from 35 to 1 cal ka BP.

The results revealed five different stages of ISM evolution in this region: from 35 to 29.8 cal ka BP, the relative strong ISM strength with significant fluctuations; from 29.8 to 19.2 cal ka BP, the overall gradual decreasing of ISM change; from 19.2 to 15 cal ka BP, represent the LGM with weak ISM strength; from 15 to 6.2 cal ka BP, the relative strong ISM strength; from 6.2-1 cal ka BP, the gradual weakening ISM strength again. A series of global climate events are records in our study, including in the North Atlantic 8.2 ka cold event, Heinrich 3 cold event and B/A warming event.

We suggested that both the external solar insolation and internal NH and SH temperature control the ISM evolution by impacting the cross-equatorial pressure

gradient. However, the temperature of NH and SH play the competitive influence in dominating the ISM variability at different stages, either the higher NH temperature than normal or lower SH temperature than normal would have dominated influence in ISM intensity.

Acknowledgments

We thank Zongqi Duan, Shihu Li, Huafeng Qin, Bailing Wu, Jie Yuan and Zhaoxia Jiang (Institute of Geology and Geophysics, Chinese Academy of Sciences) for instruction of magnetic test, Lu Wang, Min Zhou and Fan Yang (Sun Yat-sen University) for their assistance in field and laboratory, and Pat Munday (Montana Tech) for his assistance with technical editing. This project was supported by NSFC (Natural Science Foundation of China; grant no. 41030366 and 41672162) and Guangdong Province Introduced Innovative R&D Team of Geological Processes and Natural Disasters around the South China Sea (grant no. 2106ZT06N331). Finally, we would like to acknowledge the comments and recommendations of the reviewers who helped us to improve the quality of this work.

References

Alley, R.B., Mayewski, P.A., Sowers, T., Stuiver, M., Taylor, K.C., Clark, P.U., 1997. Holocene climatic instability: a prominent, widespread event 8200 yr ago. Geology 25, 483-486.

An, Z.S., Clemens, S.C., Shen, J., Qiang, X.K., Zhang, D.J., Sun,Y.B., Prell, W.L., Luo, J.J., Wang, S.M., Xu, H., Cai, Y.J., Zhou, W.J., Liu, X.D., Liu, W.G., Shi,

Z.G., Yan, L.B., Xiao, X.Y., Chang, H., Wu, F., Ai, L., Lu, F.Y., 2011. Glacial-Interglacial Indian Summer Monsoon Dynamics. Science. 333, 719-723.

Anderson, R.F., Ali, S., Bradtmiller, L.I., Nielsen, S.H., Fleisher, M.Q., Anderson, B.E., Burckle, L.H., 2009. Wind-driven upwelling in the Southern ocean and the deglacial rise in atmospheric CO_2. Science. 323, 1443-1448.

Bard, E., Rostek, F., Turon, J.L., Gendreau, S., 2001. Hydrological impact of Heinrich events in the subtropical northeast Atlantic. Science. 289, 1321-1324.

Barker, S., Diz, P., Vautravers, M.J., Pike, J., Knorr, G., Hall, I.R., Broecker, W.S., 2009. Interhemispheric Atlantic seesaw response during the last deglaciation. Nature. 457, 1097-1102.

Bintanja, R., Oldenborgh, G. J., Drijfhout, S.S., Wouters, B., Katsman, C.A., 2013. Important role for ocean warming and increased ice-shelf melt in Antarctic sea-ice expansion. Nature Geosci. 6, 376-379.

Blaauw, M., Christen, J.A., 2011. Flexible paleoclimate age-depth models using anautoregressive gamma process. Bayesian Anal. 6, 457-474.

Blott, S. J., Pye, K., 2001. Gradistat: A grain size distribution and statistics package for the analysis of unconsolidated sediments. Earth Surface Processes and Landforms 26, 1237-1248.

Blunier, T., Brook, E.J., 2001. Timing of millennial-scale climate change in Antarctica and Greenland during the Last Glacial Period. Science. 291, 109-121.

Broecker, W., Bond, G., Klas, M., Clark, E., McManus, J., 1992. Origin of the northern Atlantic's Heinrich events. Clim. Dyn. 6, 265-273.

580 Cai, Y.J., Fung, I.Y., Edwardsd, R.L., An, Z.S., Cheng, H., Leef, J.E., Tan, L.C.,
581 Sheng, C.C., Wang, X.F., Dayc, J.A., Zhou, W.J., Kellyd, M.J., Chiang, J. C. H.,
582 2015. Variability of stalagmite-inferred Indian monsoon precipitation over the past
583 252,000 y. PNAS. 112, 2954-2959.
584 Caley, T., Zaragosi1, S., Bourget, J., Martinez, P., Malaizé, B., Eynaud, F., Rossignol,
585 L., Garlan, T., Zimmermann, N. E., 2013. Southern Hemisphere imprint for Indo-
586 Asian summer monsoons during the last glacial period as revealed by Arabian Sea
587 productivity records. Biogeosci. 10, 7347-7359.
588 Chen, S. T., Wang, Y. J., Cheng, H., Edwards, R. L., Wang, X. F., Kong, X. G., Liu,
589 D. B., 2016. Strong coupling of Asian Monsoon and Antarctic climates on
590 suborbital timescales. Scientific Reports 6:32995, DOI: 10.1038/srep32995
591 Chen, X.M., Chen，F.H., Zhou, A.F., Huang, X.Z., Tang, L.Y., Wu, D., Zhang, X.J.,
592 Yu, J.Q., 2014. Vegetation history, climatic changes and Indian summer monsoon
593 evolution during the Last Glaciation (36,400-13,400 cal yr BP) documented by
594 sediments from Xingyun Lake, Yunnan, China. Palaeogeogr. Palaeocl. Palaeoecol.
595 410, 179-189.
596 Chiang, J.C.H., Bitz, C.M., 2005. Influence of high latitude ice cover on the marine
597 Intertropical Convergence Zone . Cli. Dyn. 25, 477-496.
598 Clemens, S.C., Prell, W.L., 2003. A 350,000 year summer-monsoon multi-proxy
599 stack from the Owen Ridge, Northern Arabian Sea. Marine Geo. 201, 35-51.
600 Dahl, K.A., Broccoli, A.J., Stouffer, R.J., 2005. Assessing the role of North Atlantic
601 freshwater forcing in millennial scale climate variability: a tropical Atlantic

perspective. Cli. Dyn. 24, 325-346.

Davison, W. and Seed, G., 1983. The kinetics of oxidation of ferrous iron in synthetic and natural waters, Geochim. Cosmochim. Acta. 47, 67-69.

Deaton, B.C., Balsam, W.L., 1991. Visible spectroscopy, a rapid method for determing hematite and geothite concentration in geological materials. J. Sedi. Res. 61, 628-632.

Deng, C.L., Zhu, R.X., Jackson, M.J., Verosub, K.L., Singer, M.J., 2001. Variability of the temperature-dependent susceptibility of the Holocene eolian deposits in the Chinese loess plateau: a pedogenesis indicator. Phys. Chem. Earth. 26, 873-878.

Dentón, G.H., Anderson, R.F., Toggweiler, R. F., Edwards, R. F., Schaefer, M., Putna, A.E., 2010. The Last Glacial Termination. Science. 328, 1652-1656.

Deplazes, G., Lückge, A., Peterson, L.C., Timmermann, A., Hamann, Y., Hughen, K. A., Röhl6, U., Laj, C., Cane, M.A., Sigman, D.M., Haug, G.H., 2013. Links between tropical rainfall and North Atlantic climate during the last glacial period. Nature Geosci. 6 (3), 213-217.

Doberschütz, S., Frenzel, P., Haberzettl, T., Kasper, T., Wang, J., Zhu, L.P., Daut, G., Schwalb, A., Mausbacher., 2014. Monsoonal forcing of Holocene paleoenvironmental change on the central Tibetan Plateau inferred using a sediment record from Lake Nam Co (Xizang, China). J Paleolimnol. 51, 253-266.

Duan, Z.Q., Liu, Q.S., Yang, X.Q., Gao, X., Su, Y.L. 2014. Magnetism of the Huguangyan Maar Lake sediments, Southeast China and its paleoenvironmental

623 implications. Palaeogeogr. Palaeocl. Palaeoecol. 395, 158-167.
624 Engstrom, D.R. and Wright, H.E., 1984. Chemical stratigraphy of lake sediments as a
625 record of environmental change. IN: Haworth, E. Y. and Lund, W. G. (eds), Lake
626 Sediments and Environmental History. pp.11-67. Leicester University Press,
627 Leicester.
628 EPICA Community Members, 2006. One-to-one coupling of glacial climate
629 variability in Greenland and Antarctica. Nature 444, 195-198.
630 Fleitmann, D., Burns, S.J., Mudelsee, M., Neff, U., Kramers, J., Mangini, A., Matter,
631 A. 2003. Holocene Forcing of the Indian Monsoon Recorded in a Stalagmite from
632 Southern Oman. Science. 300, 1737-1739.
633 Folk, R.L., Ward, W.C., 1957. Brazos River bar: a study in the significance of grain-
634 size parameters. J. Sediment. Petrol. 27, 3-26.
635 Frierson, D.M.W., Hwang, Y.T., Fuckar, N.S., Seager, R., Kang, S.M., Donohoe, A.,
636 Maroon, E.A., Liu, X.J., Battisti, D.S., 2013. Contribution of ocean overturning
637 circulation to tropical rainfall peak in the Northern Hemisphere. Nature Geosci. 6,
638 940-944.
639 Gent, P.R., 2016. Effects of Southern Hemisphere wind changes on the meridional
640 overturning circulation in ocean models.Annu. Rev. Mar. Sci. 8, 79-94.
641 Ghil, M., Allen, R. M., Dettinger, M. D., Ide, K., Kondrashov, D., Mann, M. E.,
642 Robertson, A., Saunders, A., Tian, Y., Varadi, F., Yiou, P., 2002. Advanced
643 spectral methods for climatic time series, Reviews of Geophysics 40(1), 3.1-3.41,
644 10.1029/2000RG000092.
645 Govil, P. , Naidu, P.D., 2011. Variations of Indian monsoon precipitation during the
646 last 32 kyr reflected in the surface hydrography of the Western Bay of Bengal.

647 Quat. Sci. Rev. 30, 3871-3879.
648 Grootes, P.M., Stuiver, M., White, J.W.C., Johnsen, S., Jouzel, J., 1993. Comparison
649 of oxygen isotope records from the GISP2 and GRIP Greenland ice cores. Nature.
650 366, 552-554.
651 Hammer, Ø., Harper, D. A. T., Ryan, P. D., 2001. Past: paleontological statistics
652 software package for education and data analysis. Palaeontologia Electronica 4(1),
653 art. 4: 9pp., 178kb.
654 Hemming, S. R., 2004. Heinrich events: Massive late Pleistocene detritus layers of the
655 North Atlantic and their global climate imprint. Reviews of Geophysics 42,
656 RG1005, doi:10.1029/2003RG000128
657 Hong, Y.T., Hong, B., Lin, Q.H., Yasuyuki, S., Hirotab, M., Zhu, Y.T., Leng, X.T.,
658 Wang, Y., Wang, H., Yi, L., 2005. Inverse phase oscillations between the East
659 Asian and Indian Ocean summer monsoons during the last 12000 years and paleo-
660 El Nin~o. Earth Planet. Sci. Lett. 231, 337-346.
661 Hu, S. Y., Goddu, S.R., Herb, C., Appel, E., Gleixner, G., Wang, S.M., Yang, X. D.,
662 Zhu, X.H., 2015. Climate variability and its magnetic response recorded in a
663 lacustrine sequence in Heqing basin at the SE Tibetan Plateau since 900 kyr.
664 Geophys. J. Int. 201, 444-458.
665 Hu, S.Y., Goddu, S.R., Appel, E., Verosub, K., 2007. Fine-tuning of age integrating
666 magnetostratigraphy, radiocarbon dating and carbonate cyclicity: example of
667 lacustrine sediments from Heqing basin (Yunnan, China) covering the past 1 Myr,
668 J. Asian Earth Sci. 30, 423-432.
669 Hu, S.Y., Goddu, S.R., Appel, E., Verosub, K., Yang, X.D., Wang, S.M., 2005.
670 Palaeoclimatic changes over past one million years derived from lacustrine
671 Sediments of Heqing Basin (Yunnan, China), Quatern. Int. 136, 123-129.
672 Huang, C., Wei, G.J., Ma, J.L., Liu, Y., 2016. Evolution of the Indian summer

673 monsoon during the interval 32.7–11.4 cal. kyr BP: Evidence from the Baoxiu
674 peat, Yunnan, southwest China. J. Asian Ear. Sci. 131,72-80.
675 Jiang, X.Y., He, Y.Q., Shen, C.C., Lee, S.Y., Yang, B., Lin, K., Li, Z.Z., 2014.
676 Decoupling of the East Asian summer monsoon and Indian summer monsoon
677 between 20 and 17 kyr. Quat. Res. 82, 146-153.
678 Jiang, Z.X. and Liu Q.S., 2016. Quantification of hematite and its climatic
679 significances. Quat. Sci. 36, 676-689. (in Chinese)
680 Jo, K.N., Woo, K.S., Yi, S., Yang, D.Y., Lim, H.S., Wang, Y.J., Cheng, H., Edwards,
681 R.L., 2014. Mid-latitude interhemispheric hydrologic seesaw over the past 550,000
682 years. Nature 508, 378-382.
683 Jouzel, J. et al, 2007. Orbital and millennial Antarctic climate variability over the past
684 800,000 years. Science 317, 793 – 796.
685 Kalnay, E., Kanamitsu, M., Kistler, R., Collins, W., Deaven, D., Gandin, L., Iredell,
686 M., Saha, S., White, G., Woollen, J., Zhu, Y., Chelliah, M., Ebisuzaki, W.,
687 Higgins, W., Janowiak, J., Mo, K.C., Ropelewski, C., Wang, J., Leetmaa, A.,
688 Reynolds, R., Jenne, R., Joseph, D., 1996. The NCEP/NCAR 40-year reanalysis
689 project. Bull. Am. Meteorol. Soc. 77, 437-471.
690 King, J.W., Channell, J.E.T., 1991. Sedimentary magnetism, environmental
691 magnetism, and magnetostratigraphy. Rev. Geophys. 29, 358-370.
692 Knutti, R., Fluckiger, J., Stocker, T.F., Timmermann, A., 2004. Strong hemi-spheric
693 coupling of glacial climate through freshwater discharge and ocean circulation.
694 Nature. 430, 851-856.

695 Kornfeld, D., Sonntag, B.L., Gast, S., Matthes, J., Ratschbacher, L., Pfänder, J.A.,
696 Eckert, S., Liu, D.L., Appel, E., Ding, L., 2014. Apparent paleomagnetic rotations
697 reveal Pliocene-Holocene internal deformation of the Tengchong Block,
698 southeastern Tibetan Plateau. J. Asian Ear. Sci. 96, 1-16.
699 Laskar, J., Robutel, P., Joutel, F., Gastineau, M., Correia, A.C.M., Levrard, B., 2004.
700 A long term numerical solution for the insolation quantities of the Earth. Astron.
701 Astrophys. Manuscr. 428, 261-285.
702 Li, D.M., Li, Q., Chen, W.J., 2000. Volcanic activities in the Tengchong volcano area
703 since Pliocene. Acta Petrologica Sinica. 16, 362-370. (in Chinese)
704 Li, H, Y,, Zhang, H. C., Chen, G. J., Chang, F. Q., Duan, L. Z., Wang, J. Y., Lu, H.
705 B., Wu, H., Hu, K., 2017. The Grain Size Distribution Characteristics of Surface
706 Sediments from Plateau Lakes in Yunnan Province and Their Environmental
707 Significances. Acta Sedimentologica Sinica 35(3), 499-507 (in Chinese)
708 Liu, J.Q., Lu, H.Y., Negendank, J., Mingram, J., Luo, X.J., 2000. Periodicity of
709 Holocene climatic variations in the Huguangyan Maar Lake. Chin. Sci. Bull. 45,
710 1712-1717.
711 Liu, S.Z., Deng, C.L., Xiao, j., Li, J.H., Paterson G.A., Chang, L., Yi, L., Qin, H.f.,
712 Zhu, R.X., 2016. High-resolution enviromagnetic records of the last deglaciation
713 from Dali Lake, Inner Mongolia. Palaeogeogr. Palaeocl. Palaeoecol. 454, 1-11.
714 Maher, B. A., 1988, Magnetic properties of some synthetic sub-micron magnetites,
715 Geophys. J., 94, 83-96.
716 Marshall, J., Donohoe, A., Ferreira, M., McGee, D., 2014.The ocean's role in setting
717 the mean position of the Inter-Tropical Convergence Zone. Clim. Dyn. 42, 1967-
718 1979.

719 Marzocchi, A., Jansen, M.F., 2017. Connecting Antarctic sea ice to deep-ocean
720 circulation in modern and glacial climate simulations. Geophys.Res. Lett., 44,
721 6286-6295.
722 Mcgee, D., Donohoe, A., Marshall, J., Ferreira, D., 2014. Changes in ITCZ location
723 and cross-equatorial heat transport at the Last Glacial Maximum, Heinrich Stadial
724 1, and the mid-Holocene. Earth Planet. Sci. Lett. 390, 69-79.
725 Nesbitt, H.W., Young, G.M., 1982. Early Proterozoic climates and plate motions
726 inferred from major element chemistry of lutites. Nature. 299, 715-717.
727 Nowaczyk, N.R., Minyuk, P., Melles, M., Brigham-Grette, J., Glushkova, O., Nolan,
728 M., Lozhkin, A.V., Stetsenko, T.V., Andersen, P.M., Forman, S.L., 2002.
729 Magnetostratigraphic results from impact crater Lake El'gygytgyn, northeastern
730 Siberia: a 300 kyr long highresolution terrestrial palaeoclimatic record from the
731 Arctic. Geophys. J. Int. 150, 109-126.
732 Pedro, J.B., Ommen, T.D.V., Rasmussen, S.O., Morgan, V.I., 2011. The last
733 deglaciation: timing the bipolar seesaw. Clim. Past. 7, 671-683.
734 Qin, X. G., Cai, B. G, Liu, T. S., 2005. Loess record of the aerodynamic environment
735 in the east Asia monsoon area since 60,000 years before present. Journal of
736 Geophysical Research 110, B01204, doi:10.1029/2004JB003131.
737 Rashid, H., England, E., Thompson, L., Polyak, L., 2011. Late Glacial to Holocene
738 Indian Summer Monsoon Variability Based upon Sediment Records Taken from
739 the Bay of Bengal. Terr. Atmos. Ocean. Sci. 22, 215-228.
740 Rawat, S., Gupta, A.K., Srivastava, P., Sangode, S.J., Nainwal, H.C., 2015. A 13000

741 year record of environmental magnetic variations in the lake. Palaeogeogr.
742 Palaeocl. Palaeoecol. 440, 116-127.
743 Reimer, P. J., Baillie, M.G.L., Bard, E., Bayliss, A ., Beck, J. W., Blackwell, P.G.,
744 Ramsey, C.B., Buck, C.E., Burr, G.S., Edwards, R.L., Friedrich, M., Grootes, P.M,
745 Guilderson, T.P., Heaton, T.J., Hogg, A.G., Hughen, K.A., Kaiser, K.F., Kromer,
746 B., McCormac, F.B., Manning, S.W., Reimer, R.W., Richards, D.A., Southon,
747 J.R., Talamo, S., Turney, C.S.M., Plicht, J., Weyhenmeyer, C.E., 2009. IntCal09
748 and Marine09 radiocarbon age calibration curves, 0-50,000 years cal BP.
749 Radiocarbon. 51, 11-50.
750 Rosales, L.A.C., Jennerjahn, T., Tharammal, T., Meyer, V., Lückge, A., Paul, A.,
751 Schefuß, E., 2014. Evolution of the Indian Summer Monsoon and terrestrial
752 vegetation in the Bengal region during the past 18 kyr. Quat. Sci. Rev. 102, 133-
753 148.
754 Schulz, H., Rad, U.V., Erlenkeuser, H., 1988. Correlation between Arabian Sea and
755 Greenland climate oscillations of the past 110,000 years. Nature. 393, 54-57.
756 Sun, Q.L., Wang, S.M., Zhou, J., Chen, Z.Y., Shen, J., Xie, X.P., Wu, F., Chen, P.,
757 2010. Sediment geochemistry of Lake Daihai, north-central China: implications for
758 catchment weathering and climate change during the Holocene, J. Paleolimnol. 43,
759 75-87.
760 Thompson, R. and Oldfield, F., 1986. Environmental Magnetism. Allen and Unwin,
761 London.

762 Vellinga, M. and Wood, R.A., 2002. Global climatic impacts of a collapse of the
763 Atlantic Thermohaline circulation. Cli. Dym. 54, 251-267.
764 WAIS Divide Project Members, 2015. Precise interpolar phasing of abrupt climate
765 change during the last ice age. Nature 520, 661–664.
766 Wang, Q., Yang, X.D., Anderson, J.N., Zhang, E.L., Li, Y.L., 2014. Diatom response
767 to climate forcing of a deep, alpine lake (Lugu Hu,Yunnan, SW China) during the
768 Last Glacial Maximum and its implications for understanding regional monsoon
769 variability. Quat. Sci. Rev. 86, 1-12.
770 Wang, Q., Yang,X.D., Anderson, N.J., Zhang, E.L., Li, Y.L., 2014. Diatom response
771 to climate forcing of a deep, alpine lake (Lugu Hu, Yunnan, SW China) during the
772 Last Glacial Maximum and its implications for understanding regional monsoon
773 variability. Quat. Sci. Rev. 86, 1-12.
774 Wang, X.F., Auler, A.S., Edwards, R.L., Cheng, H., Cristalli, P.S., Smart, P.L.,
775 Richards, D.A., Shen, C.C., 2004. Wet periods in northeastern Brazil over the past
776 210 kyr linked to distant climate anomalies. Nature. 432, 740-743.
777 Wang, Y.F., Zhu, Y.X., Pan, H.X., Yin, Y., 2002. Environmental characteristics of an
778 acid Qinghai Lake in Tengchong, Yunnan Province. J. Lake Sci. 14, 117-124. (In
779 Chinese)
780 Wang, Y.J., Cheng, H., Edwards, R.L., He, Y., Kong, X., An, Z.S., Wu, J.Y., Kelly,
781 M.J., Dykoski, C.A., Li, X., 2005. The Holocene Asian monsoon: links to solar
782 changes and North Atlantic climate. Science 308, 854-857.
783 Weber, M.E., Clark, P.U., Kuhn, G., Timmermann, A., Sprenk, D., Gladstone, R.,

784 Zhang, X., Lohmann, G., Menviel, L., Chikamoto, M.O., Friedrich, T., Ohlwein,
785 C., 2014. Millennial-scale variability in Antarctic ice-sheet discharge during the
786 last deglaciation. Nature 510, 134-138.
787 White, A.F. and Blum A.E., 1995. Effects of climate on chemical weathering in
788 watersheds. Geochim. Cosmochim. Acta. 59, 1729-1747.
789 Wu, D., Zhou, A.F., Chen, X.M., Yu, J.Q., Zhang, J.W., Sun, H.L., 2015.
790 Hydrological and ecosystem response to abrupt changes in the Indian monsoon
791 during the last glacial, as recorded by sediments from Xingyun Lake, Yunnan,
792 China. Palaeogeogr. Palaeocl. Palaeoecol. 421, 15-23.
793 Xiao, X.Y., Shen, J.I., Haberle, S.G., Han, Y., Xue, B., Zhang, E.L., Wang, S.M.,
794 Tong, G.B., 2015. Vegetation, fire, and climate history during the last 18 500 cal a
795 BP in south-western Yunnan Province, China. J. Quat. Sci. 30, 859-869.
796 Xu, H., Zhou, X.Y., Lan, J.H., Liu, B., Sheng, E.G., Yu, K.K., Cheng, P., Wu, F.,
797 Hong, B., Yeager, K.M., Xu, S., 2015. Late Holocene Indian summer monsoon
798 variations recorded at Lake Erhai, Southwestern China. Quat. Res. 83, 307-314.
799 Xue, F., Wang, H.J., He, J.H., 2004. Interannual variability of Mascarene high and
800 Australian high and their influences on East Asian summer monsoon. J.
801 Meteorologi. Soc. Jap. 82, 1173-1186.
802 Yancheva, G., Nowaczyk, N.R., Mingram, J., Dulski, P., Schettler, G., Negendank,
803 J.F.W., Liu, J.Q., Sigman, D.M., Peterson, L.C., Haug, G.H., 2007. Influence of
804 the intertropical convergence zone on the East Asian monsoon. Nature 445, 74-77.

Yang, Y.P., Zhang, H.C., Chang, F.Q., Meng, H.W., Pan, A.D., Zheng, Z., Xiang, R., 2016. Vegetation and climate history inferred from a Qinghai Crater Lake pollen record from Tengchong, southwestern China. Palaeogeogr. Palaeocl. Palaeoecol. 461, 1-11.

Zhang, E.L., Sun, W.W., Zhao, C., Wang, Y.B., Xue, B., Shen, J., 2015. Linkages between climate, fire and vegetation in southwest China during the last 18.5 ka based on a sedimentary record of black carbon and its isotopic composition. Palaeogeogr. Palaeocl. Palaeoecol. 435, 86-94.

Zhang, E.L., Zhao, C., Xue, B., Liu, Z.H., Yu, Z.C., Chen, R., Shen, J., 2017. Millennial-scale hydroclimate variations in southwest China linked to tropical Indian Ocean since the Last Glacial Maximum. Geology 45 (5), G38309.1.

Zhang, J. W., Chen, F. H., Holmes, J. A., Li, H., Guo, X. Y., Wang, J. L., Li S., Lu Y.B., Zhao, Y, Qiang, M. R., 2011. Holocene monsoon climate documented by oxygen and carbon isotopes from lake sediments and peat bogs in China: a review and synthesis. Quat. Sci. Rev. 30, 1973-1987.

Zhao, K., Wang, Y.J., Edwards, R.L., Cheng, H., Liu, D.B., 2010. High-resolution stalagmite δ18O records of Asian monsoon changes in central and southern China spanning the MIS 3/2 transition. Earth Planet. Sci. Lett. 298, 191-198.

Zhu, X.Y., Zhang, M.L., Cheng, H., Wu, X., Edwards, R.L., 2015. Centennial- scale monsoon climate fluctuations from a stalagmite record during the mid-Holocene epoch in Fulu cave of Huaping,Yunnan, China. Environ. Earth. Sci. 74, 929-935.

826

Figure and Supplementary Captions:

Fig. 1 (A) Regional overview and location of Tengchong (ISM, Indian Summer Monsoon). The blue line and arrows showing the June–July–August mean 850-hPa streamlines during 1970–2000 (Kalnay et al., 1996; An et al., 2011) . The L–L' is the ISM route from the Bay of Bengal to Tengchong. (B) The topographic settings around TCQH Lake (from Google Earth). The circle displays the site of core. (C) The elevation change of longitudinal section along the ISM route L–L' of (A).

Fig. 2 Monthly average temperatures and precipitation distribution of Tengchong between 1971 to 2000. Most precipitation is concentrated on May-October. (Data from http://data.cma.cn/data/weatherBk.html).

Fig. 3 Age-depth model for sediment core QH4 produced using the Bacon software (Blaauw and Christen, 2011). The dark blue and black dotted lines indicate the 95% confidence intervals and the red line shows the fitting weighted mean ages. The lithology was also list in the left.

Fig. 4 Grain-size records of core QH4. The blue shaded bands show the North Atlantic 8.2 ka cold event and Heinrich event 0-3 (H0-H3); the green band represents Last Glacial Maximum period (LGM). The red shaded band shows the warm event Bølling-Allerød (B/A). The fractions of grain size <1 μm, 1.3-5 μm, 1.3-15 μm are inversely correlated with grain size 63-1000 μm. The variations of grain size fraction can be divided into five stages (a-e) labeled by dotted lines.

Fig. 5 Geochemical analysis of core QH4. The Al_2O_3, TiO_2 and the ratios of Fe_2O_3/CaO, TiO2/CaO all are consistent with chemical weathering index CIA. The green shaded band show the North Atlantic 8.2 ka cold event, Heinrich event 3 (H3) and Last Glacial maximum period (LGM). The red shaded band show the warm event Bølling-Allerød (B/A).

Fig. 6 κ-T curves for representative samples from core QH4, where the solid and dash curves represent the heating and cooling curves, respectively. In the heating process, a sharp decrease during 550-600 ℃ demonstrates the thermal unblocking of major magnetic mineral–magnetite. The notable hump at around 450-550 °C may result from the neo-formation of magnetite from iron-containing minerals silicates and clays (Deng et al., 2001). (A-C) show a weak decreasing trend after 100℃, and all the four typical samples decline after 600 ℃, indicating the composition of goethite and hematite, respectively.

Fig.7 The second derivative curves of DRS results for representative samples. The prominent peaks (green band) at about 450 nm wavelength indicate the goethite and the 580 nm indicate the hematite (Bobby and William, 1991).

Fig. 8 Environmental magnetism parameters of core QH4. The x-axis of (A-C) are plotted on a logarithmic scale, and are consistent with the HIRM and most of part show a reverse pattern with S-ratio. The green shaded band shows the North Atlantic 8.2 ka cold event, Heinrich event H3 and Last Glacial maximum period (LGM). The red shaded band shows the warm event Bølling -Allerød (B/A).

Fig. 9 Comparison of QH4 SIRM and grain size(<16um) with regional records over the past 35 ka. (A) Stalagmite oxygen isotope ($\delta^{18}O$) from Xiaobailong Cave (Cai et al., 2015) . (B) Grain size (<16mm) content from TCQH10 (Zhang et al., 2017). (C) Black carbon isotope $\delta^{13}C_{BC}$ from TCQH10 (Zhang et al., 2015). (D) K/Rb ratio from the sedment of Baoxiu peat (Huang et al., 2016). (E) Pollen percentages of cold tolerant conifers PCA-1 scores form Xingyun lake (Chen et al., 2014). (F) Stalagmite Oxygen isotope ($\delta^{18}O$) from Sangxing cave (Jiang et al., 2014). (G&H) SIRM and Grain size (1.3-5 μm) from QH4 (this paper). (I) Reflectance L^* from Arabian Sea (50-point running mean, Deplazes et al., 2013). The red shaded band show the warm event Bølling -Allerød (B/A). The green shadings show the cold events Heinrinch events (H1, H2, H3) and Last Glacial maximum (LGM) which indicate relatively weak ISM strength periods. The light yellow shading shows the warm event Bølling-Allerød (B/A), indicating relatively strong ISM strength periods.

Fig. 10 Global correlations and forcings since 35 ka. (A) Oxygen isotope ($\delta^{18}O$) from the Greenland GRIP2 ice core (Grootes et al., 1993). (B) Average summer insolation at 25□ N (Laskar et al., 2004). (C) SST reconstruction from western Bay of Bengal sediment core SK218/1(Govil and Naidu, 2011). (D&E) SIRM and Grain size (1.3-5 μm) from QH4 (this paper). (F) $\delta^{18}O$ record of Antarctica EDML ice core (EPICA community members, 2006).

Supplementary 1 The distribution of grain size.

Supplementary 2 Spectral analyses for the different proxies.

Supplementary 3 The different components comparison between our ISM proxies of FGS fraction, ARM/SIRM and the records of EDML, EDC and GISP2 (EPICA Community Members, 2006; WAIS Divide Project Members, 2015; Jouzel, J. et al, 2007). The symbols Q1-Q14 on synthesizing ISM proxy in the PC3 represent cold ISM events.

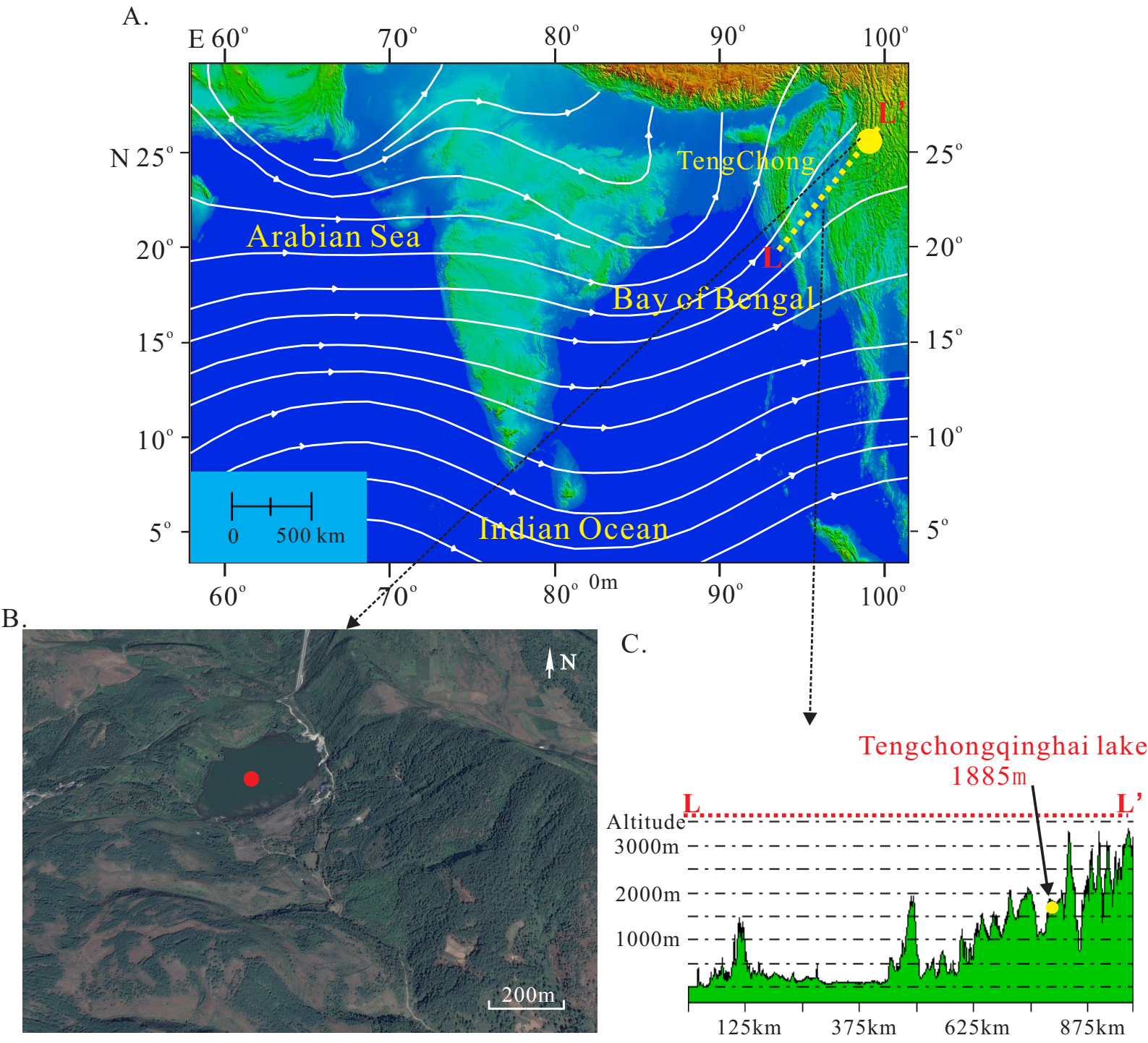
A.
E 60°
70°
80°
90°
100°
N 25°
20°
15°
10°
5°
L'
TengChong
L
Arabian Sea
Bay of Bengal
Indian Ocean
0
500 km
0m
B.
N
200m
C.
Tengchongqinghai lake
1885m
L
L'
Altitude
3000m
2000m
1000m
125km
375km
625km
875km

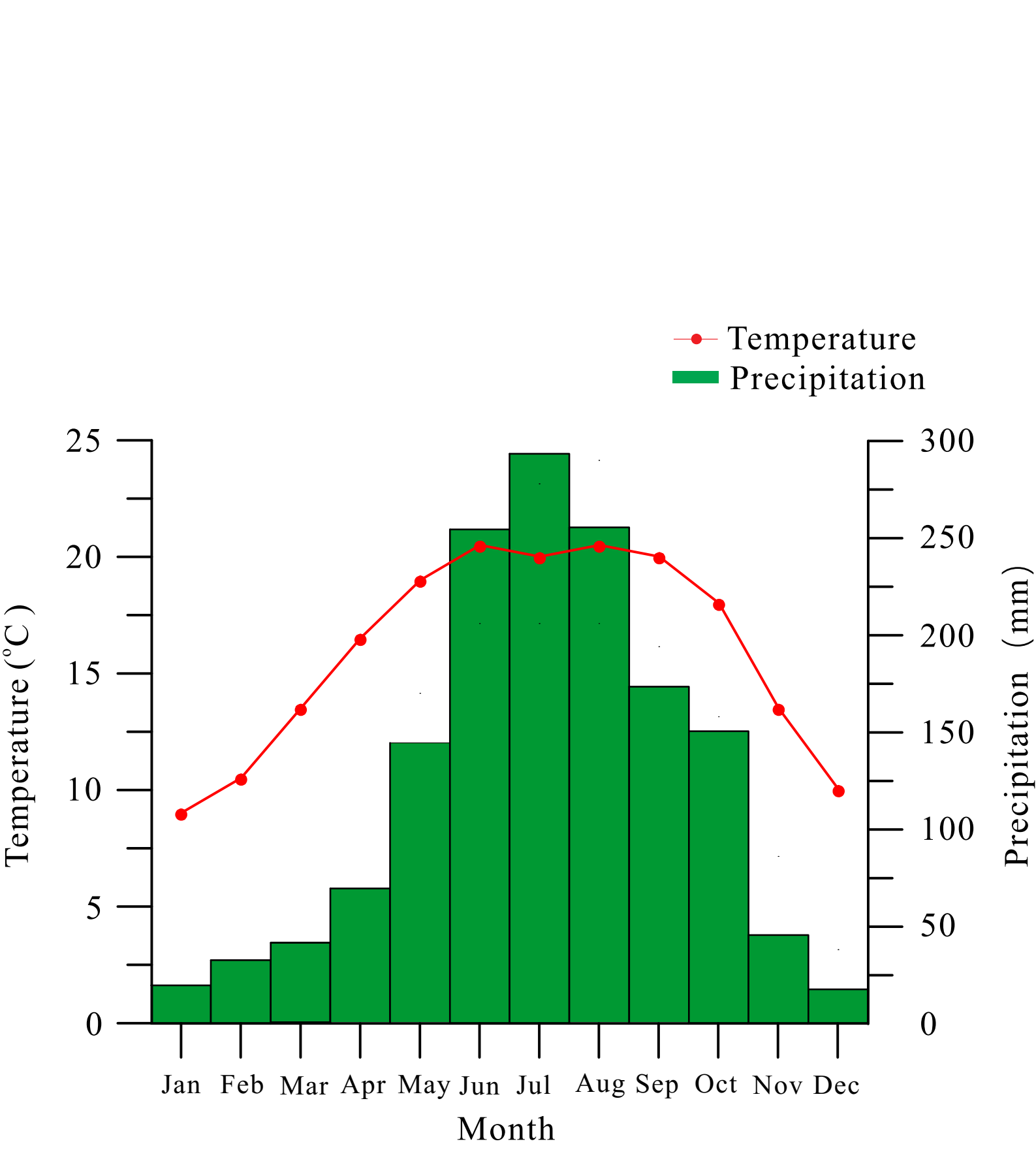
Temperature
Precipitation
25
20
15
10
5
0
Temperature (°C)
300
250
200
150
100
50
0
Precipitation (mm)
Jan
Feb
Mar
Apr
May
Jun
Jul
Aug
Sep
Oct
Nov
Dec
Month

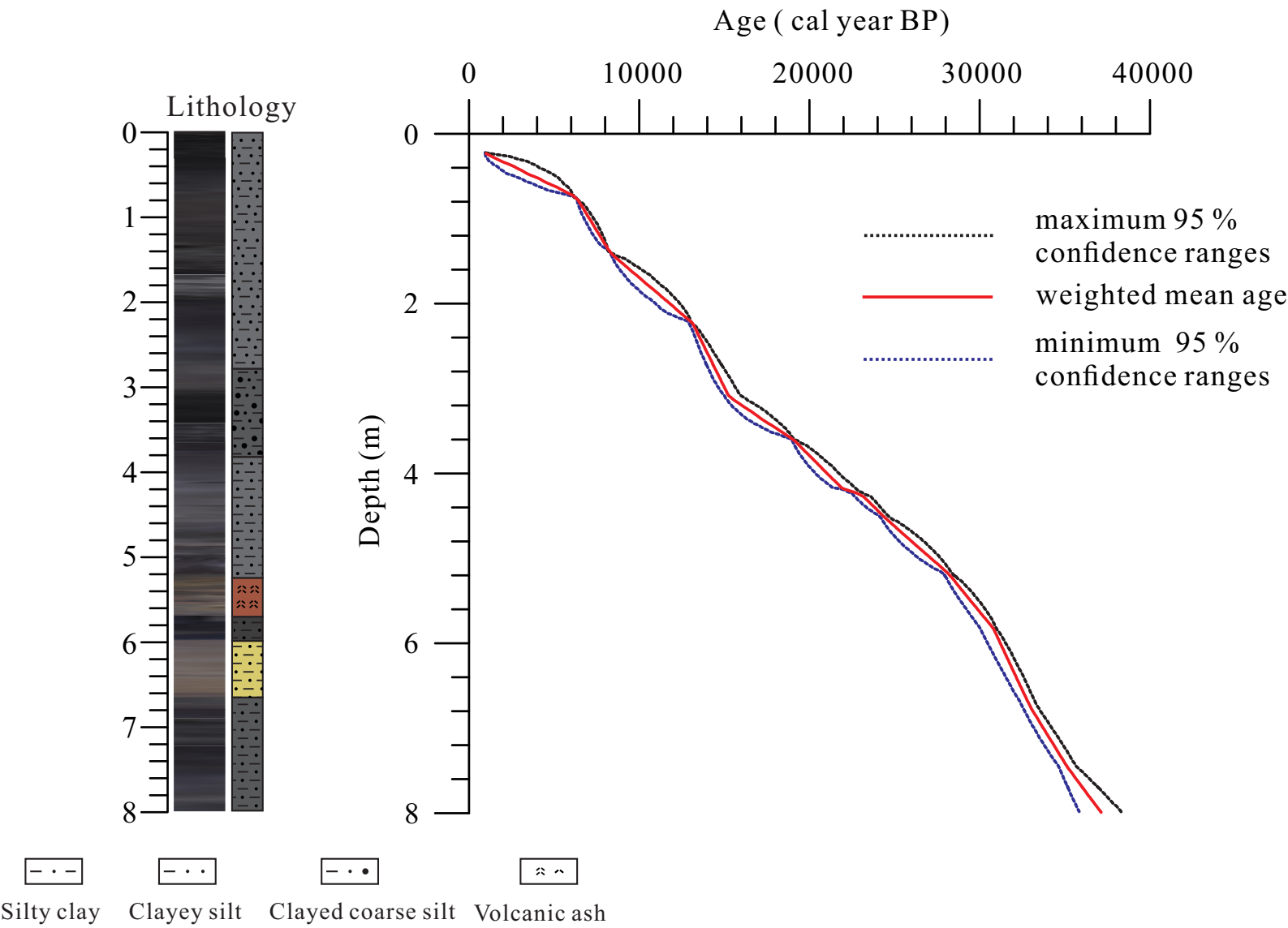
Age (cal year BP)
0
10000
20000
30000
40000
Lithology
Depth (m)
0
1
2
3
4
5
6
7
8
maximum 95 % confidence ranges
weighted mean age
minimum 95 % confidence ranges
Silty clay
Clayey silt
Clayed coarse silt
Volcanic ash

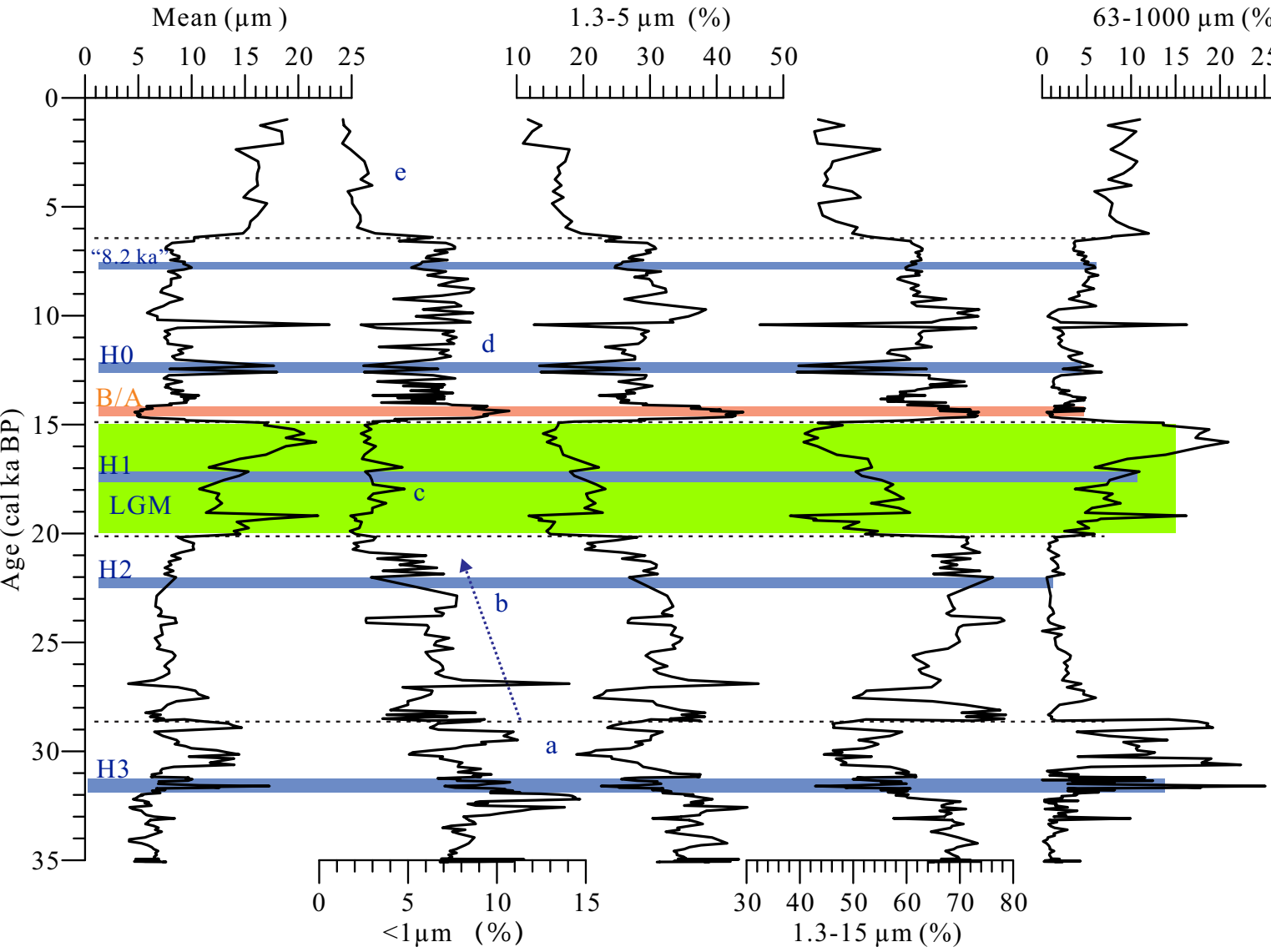
Mean (µm)
0 5 10 15 20 25
1.3-5 µm (%)
10 20 30 40 50
63-1000 µm (%)
0 5 10 15 20 25 30
Age (cal ka BP)
0
5
10
15
20
25
30
35
"8.2 ka"
H0
B/A
H1
LGM
H2
H3
a
b
c
d
e
0 5 10 15
<1µm (%)
30 40 50 60 70 80
1.3-15 µm (%)

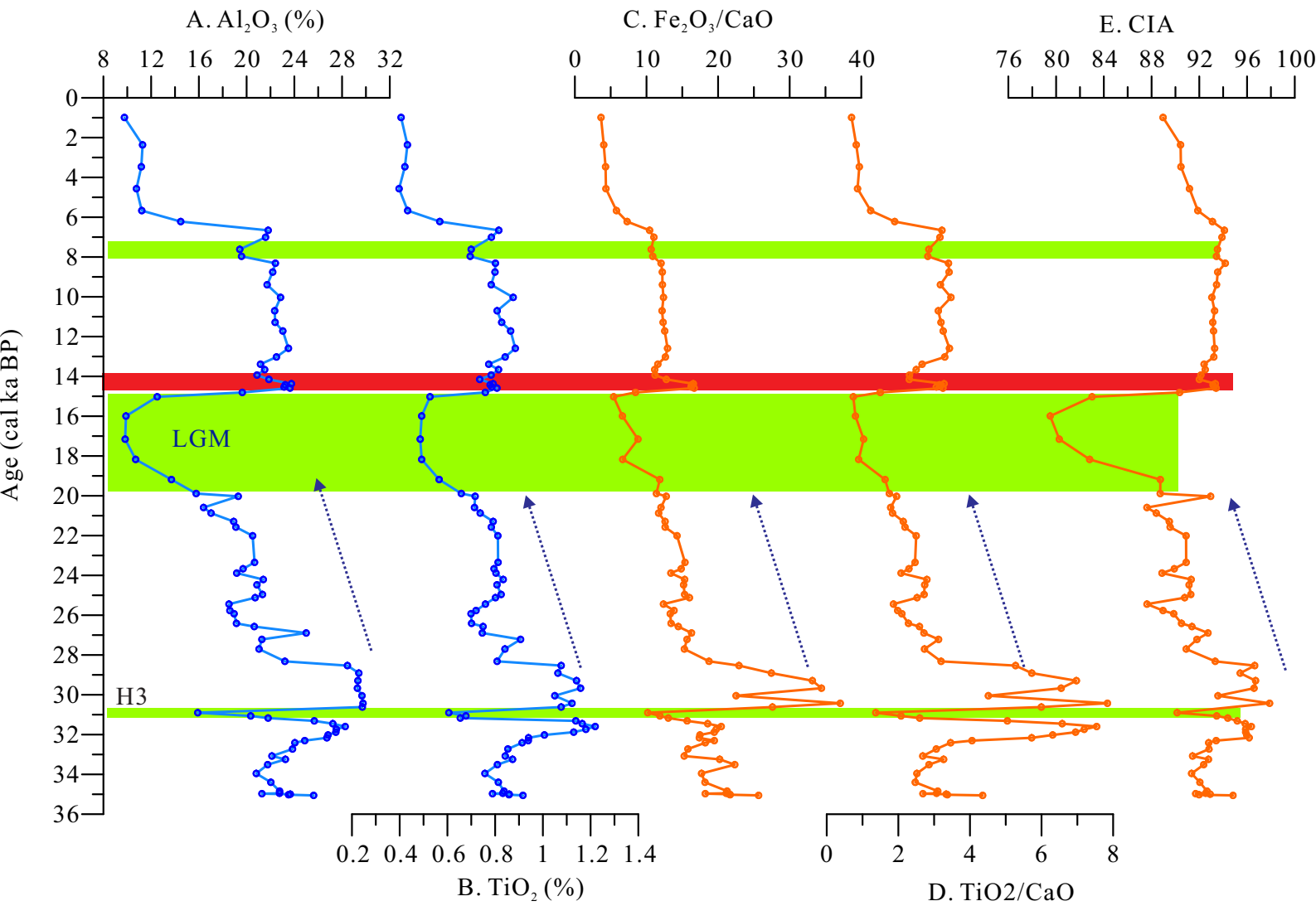
A. Al2O3 (%)
8 12 16 20 24 28 32
C. Fe2O3/CaO
0 10 20 30 40
E. CIA
76 80 84 88 92 96 100
Age (cal ka BP)
0 2 4 6 8 10 12 14 16 18 20 22 24 26 28 30 32 34 36
LGM
H3
0.2 0.4 0.6 0.8 1 1.2 1.4
B. TiO2 (%)
0 2 4 6 8
D. TiO2/CaO

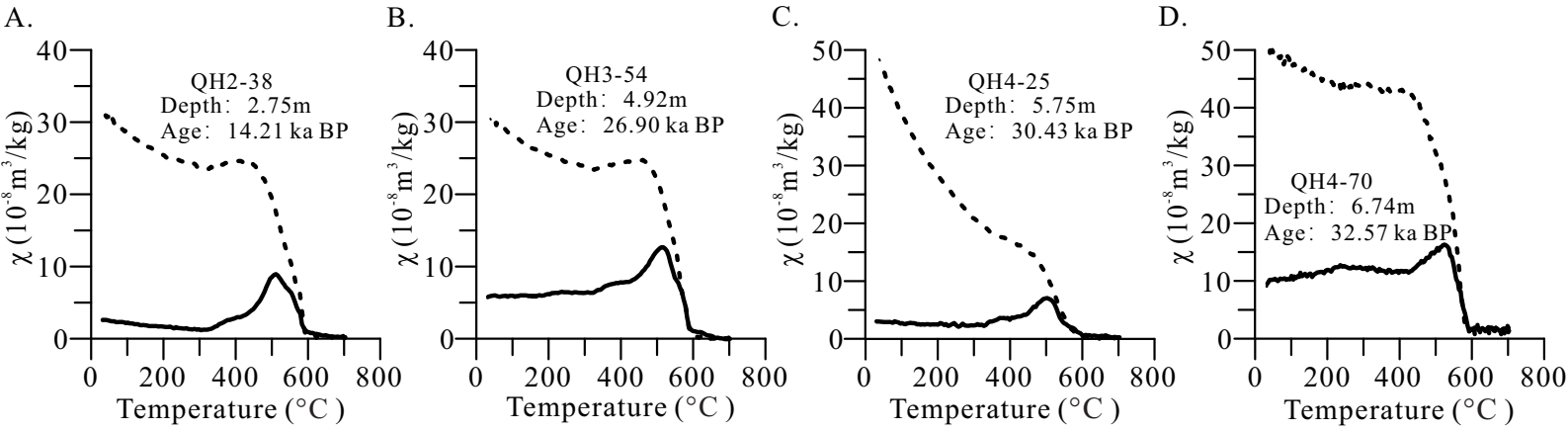
A.
QH2-38
Depth: 2.75m
Age: 14.21 ka BP
B.
QH3-54
Depth: 4.92m
Age: 26.90 ka BP
C.
QH4-25
Depth: 5.75m
Age: 30.43 ka BP
D.
QH4-70
Depth: 6.74m
Age: 32.57 ka BP
χ (10-8m3/kg)
Temperature (°C)

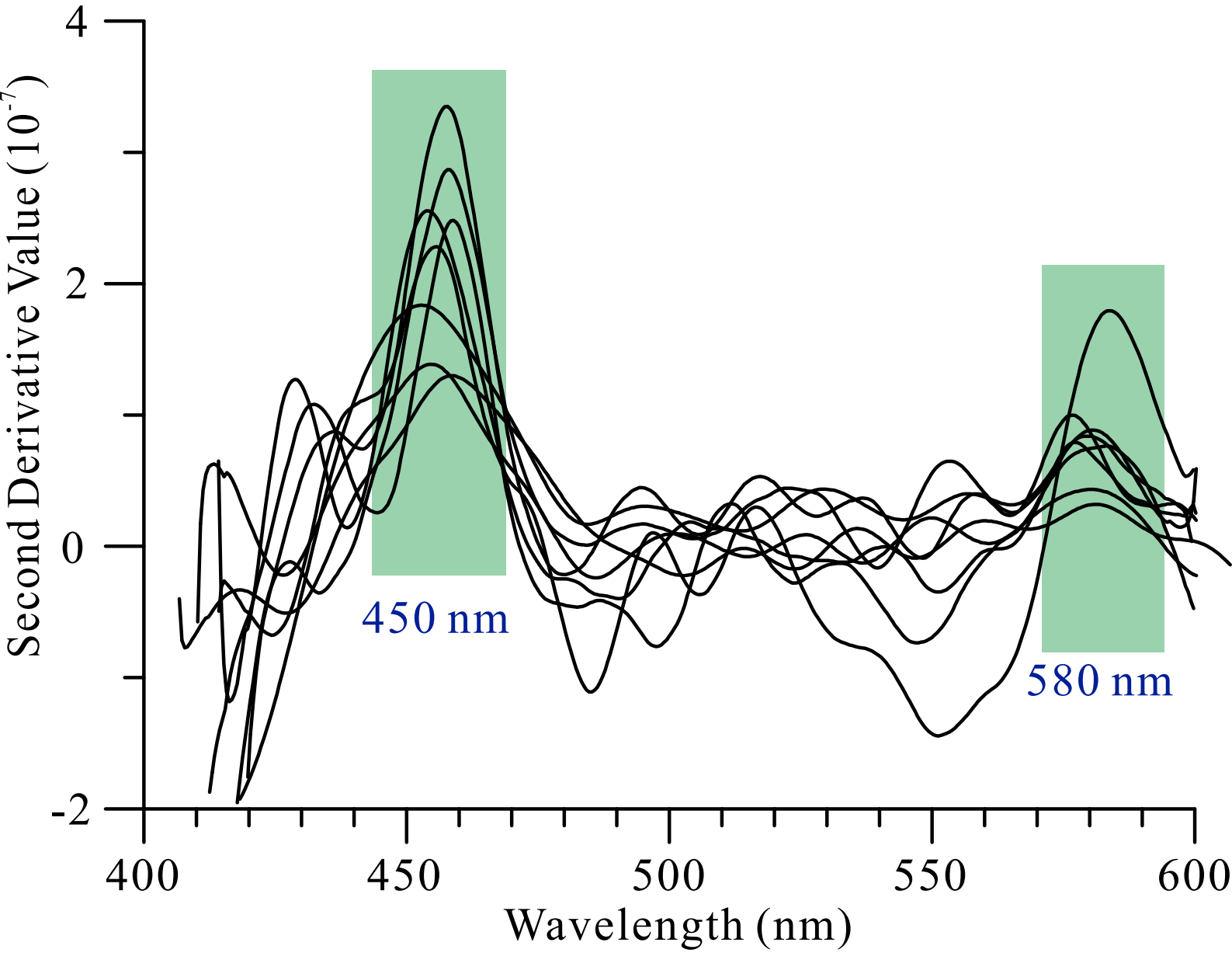
4
2
0
-2
Second Derivative Value (10^{-7})
450 nm
580 nm
400
450
500
550
600
Wavelength (nm)

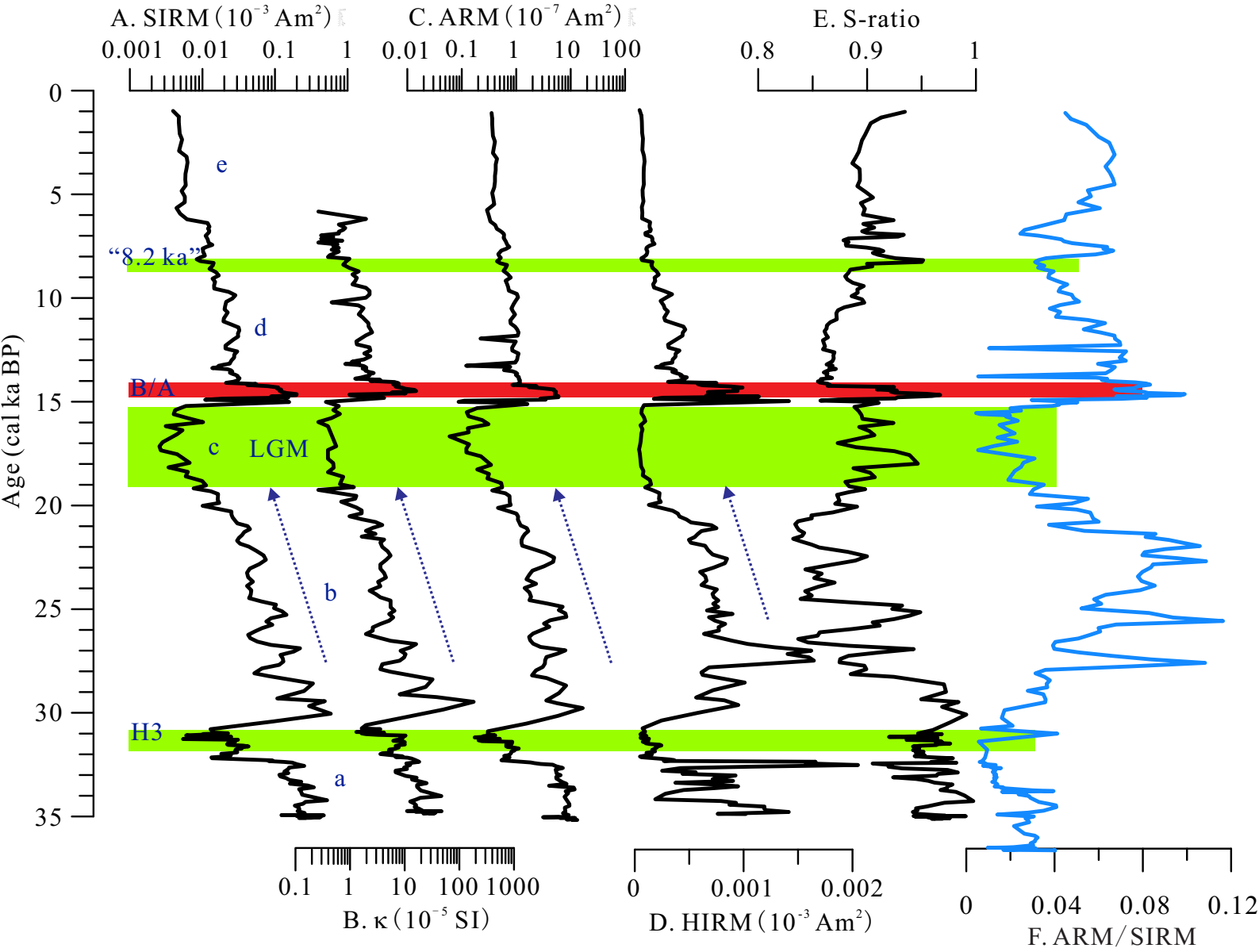
A. SIRM (10⁻³ Am²)
0.001 0.01 0.1 1
C. ARM (10⁻⁷ Am²)
0.01 0.1 1 10 100
E. S-ratio
0.8 0.9 1
Age (cal ka BP)
0 5 10 15 20 25 30 35
e
"8.2 ka"
d
B/A
c
LGM
b
H3
a
0.1 1 10 100 1000
B. κ (10⁻⁵ SI)
0 0.001 0.002
D. HIRM (10⁻³ Am²)
0 0.04 0.08 0.12
F. ARM/SIRM

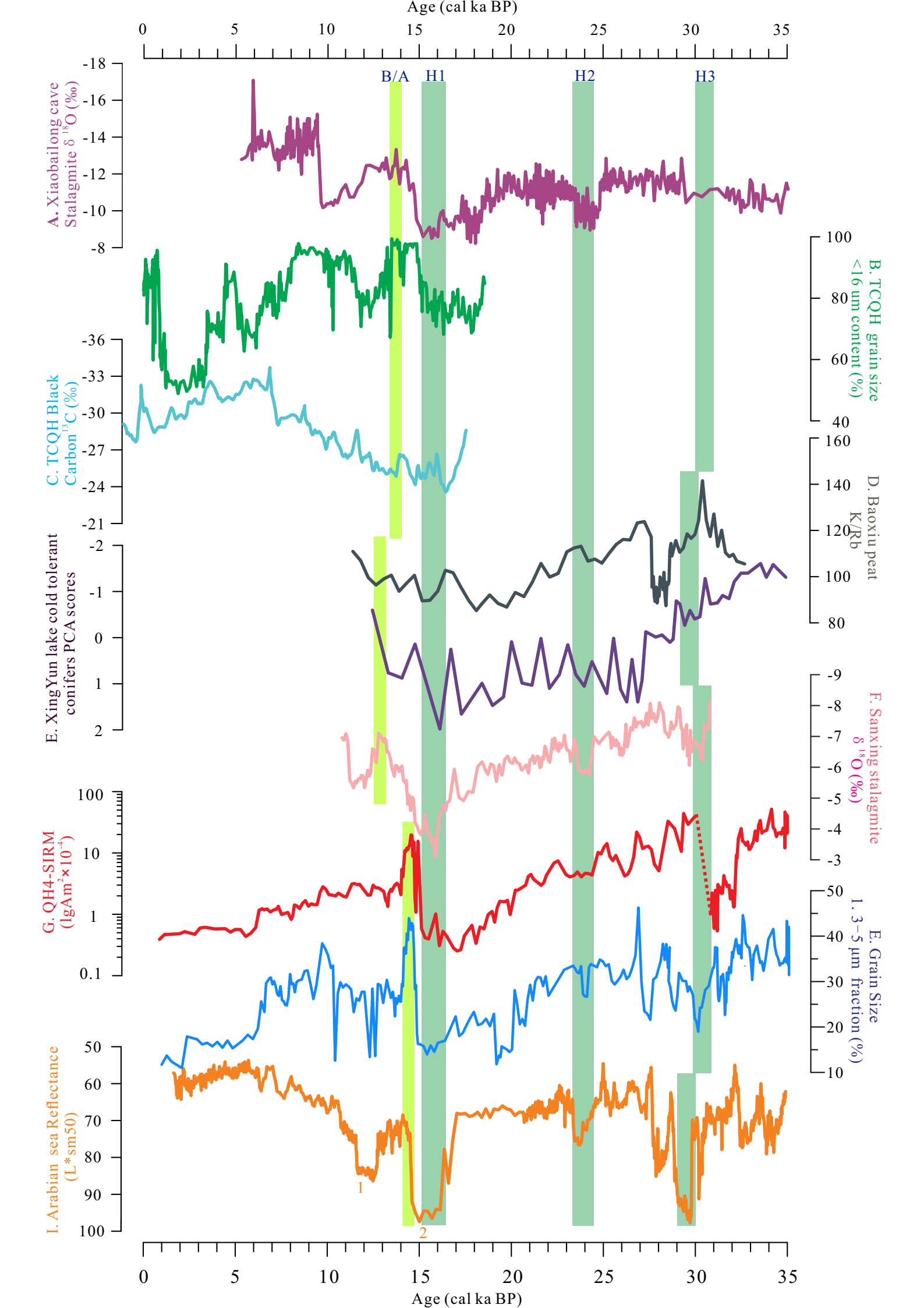
Age (cal ka BP)
0
5
10
15
20
25
30
35
B/A
H1
H2
H3
A. Xiaobailong cave Stalagmite δ18O (‰)
-18
-16
-14
-12
-10
-8
B. TCQH grain size <16 um content (%)
100
80
60
40
C. TCQH Black Carbon 13C (‰)
-36
-33
-30
-27
-24
-21
D. Baoxiu peat K/Rb
160
140
120
100
80
E. XingYun lake cold tolerant conifers PCA scores
-2
-1
0
1
2
F. Sanxing stalagmite δ18O (‰)
-9
-8
-7
-6
-5
-4
-3
G. QH4-SIRM (lgAm2×10-4)
100
10
1
0.1
E. Grain Size 1.3–5 μm fraction (%)
50
40
30
20
10
I. Arabian sea Reflectance (L*sm50)
50
60
70
80
90
100
1
2
0
5
10
15
20
25
30
35
Age (cal ka BP)

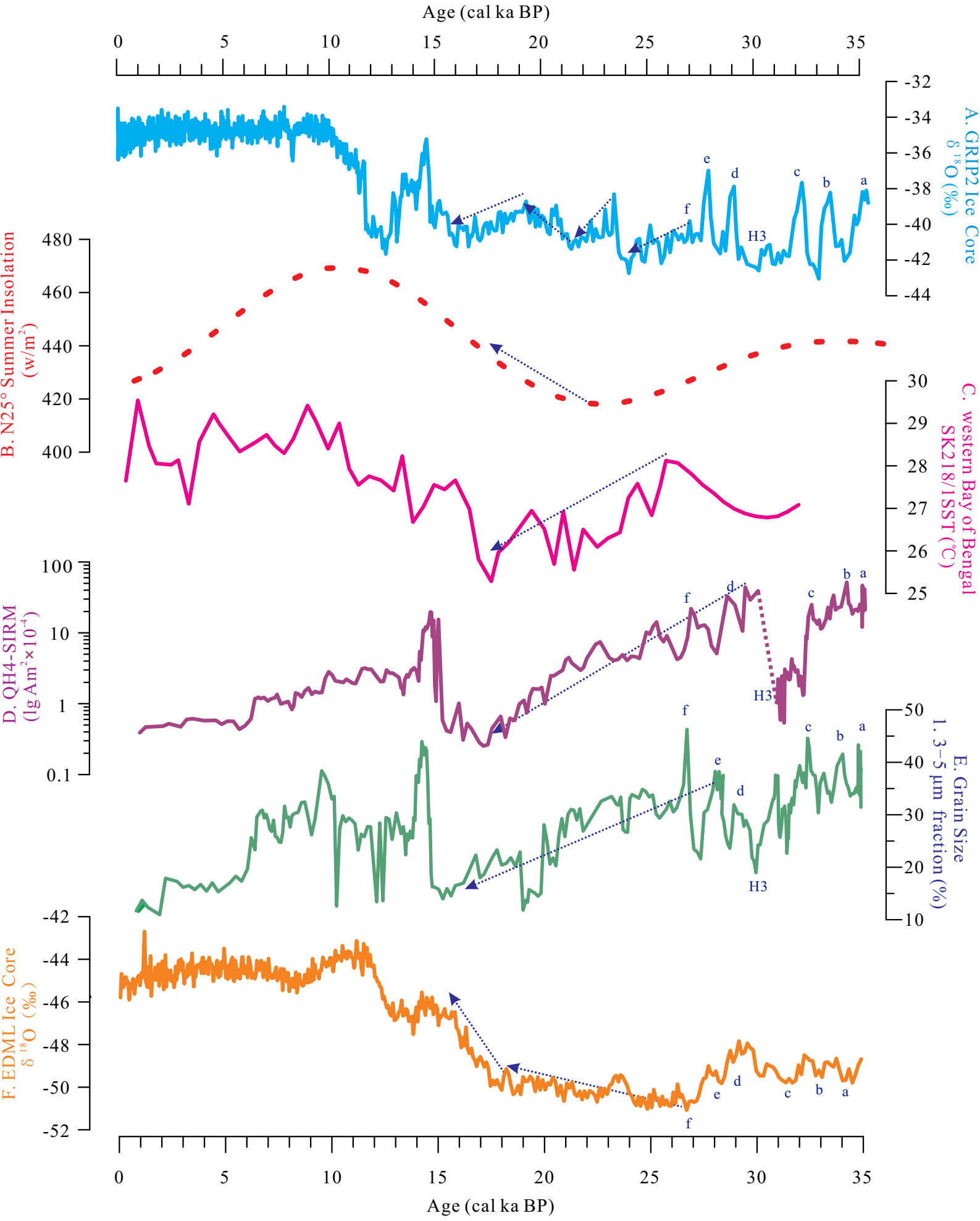
Age (cal ka BP)
0
5
10
15
20
25
30
35
A. GRIP2 Ice Core
δ 18O (‰)
-32
-34
-36
-38
-40
-42
-44
a
b
c
d
e
f
H3
B. N25° Summer Insolation
(w/m2)
480
460
440
420
400
C. western Bay of Bengal
SK218/1SST (°C)
30
29
28
27
26
25
D. QH4-SIRM
(lg Am2×10-4)
100
10
1
0.1
E. Grain Size
1. 3–5 μm fraction (%)
50
40
30
20
10
F. EDML Ice Core
δ 18O (‰)
-42
-44
-46
-48
-50
-52
Age (cal ka BP)

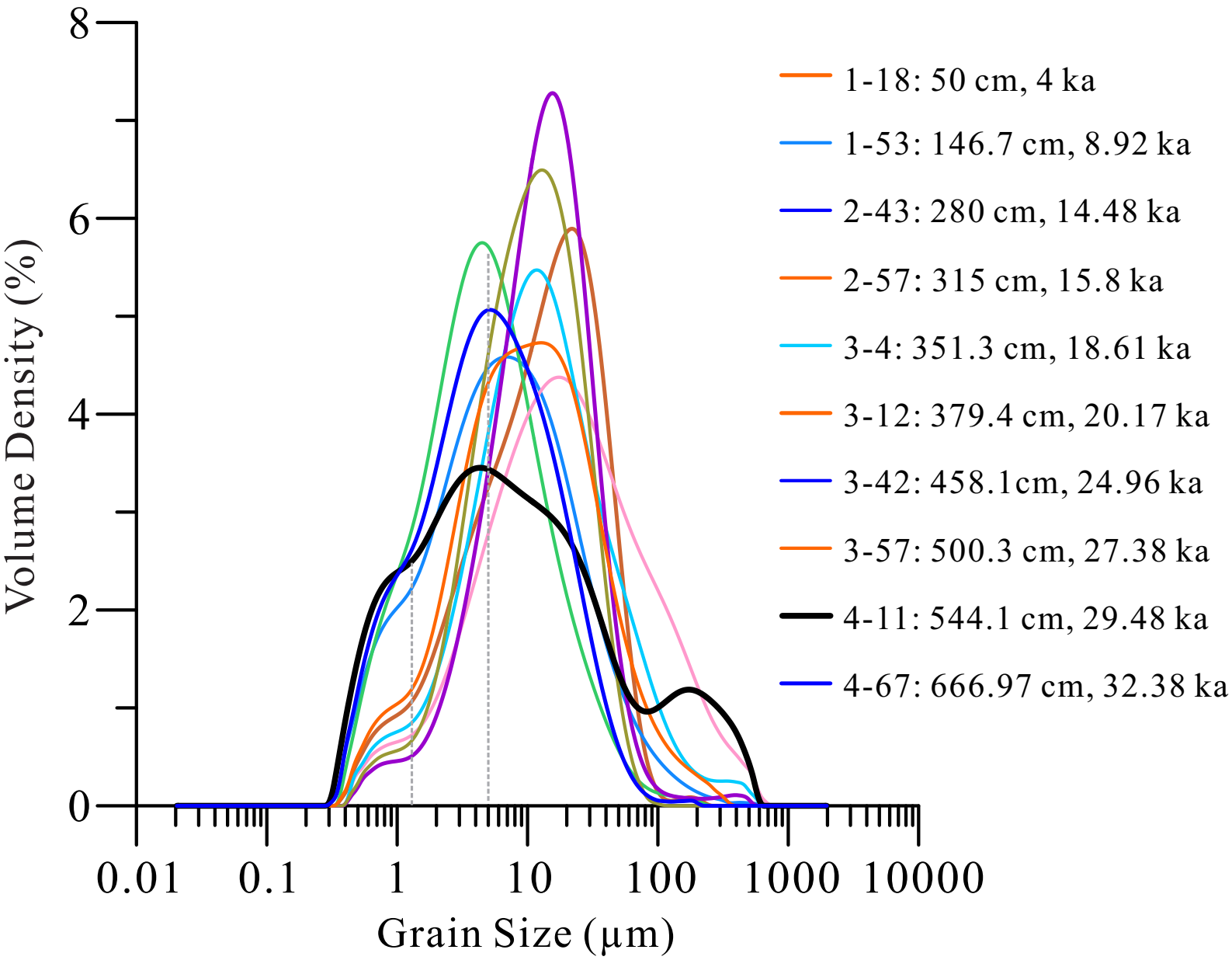
Volume Density (%)
8
6
4
2
0
0.01
0.1
1
10
100
1000
10000
Grain Size (μm)
1-18: 50 cm, 4 ka
1-53: 146.7 cm, 8.92 ka
2-43: 280 cm, 14.48 ka
2-57: 315 cm, 15.8 ka
3-4: 351.3 cm, 18.61 ka
3-12: 379.4 cm, 20.17 ka
3-42: 458.1cm, 24.96 ka
3-57: 500.3 cm, 27.38 ka
4-11: 544.1 cm, 29.48 ka
4-67: 666.97 cm, 32.38 ka

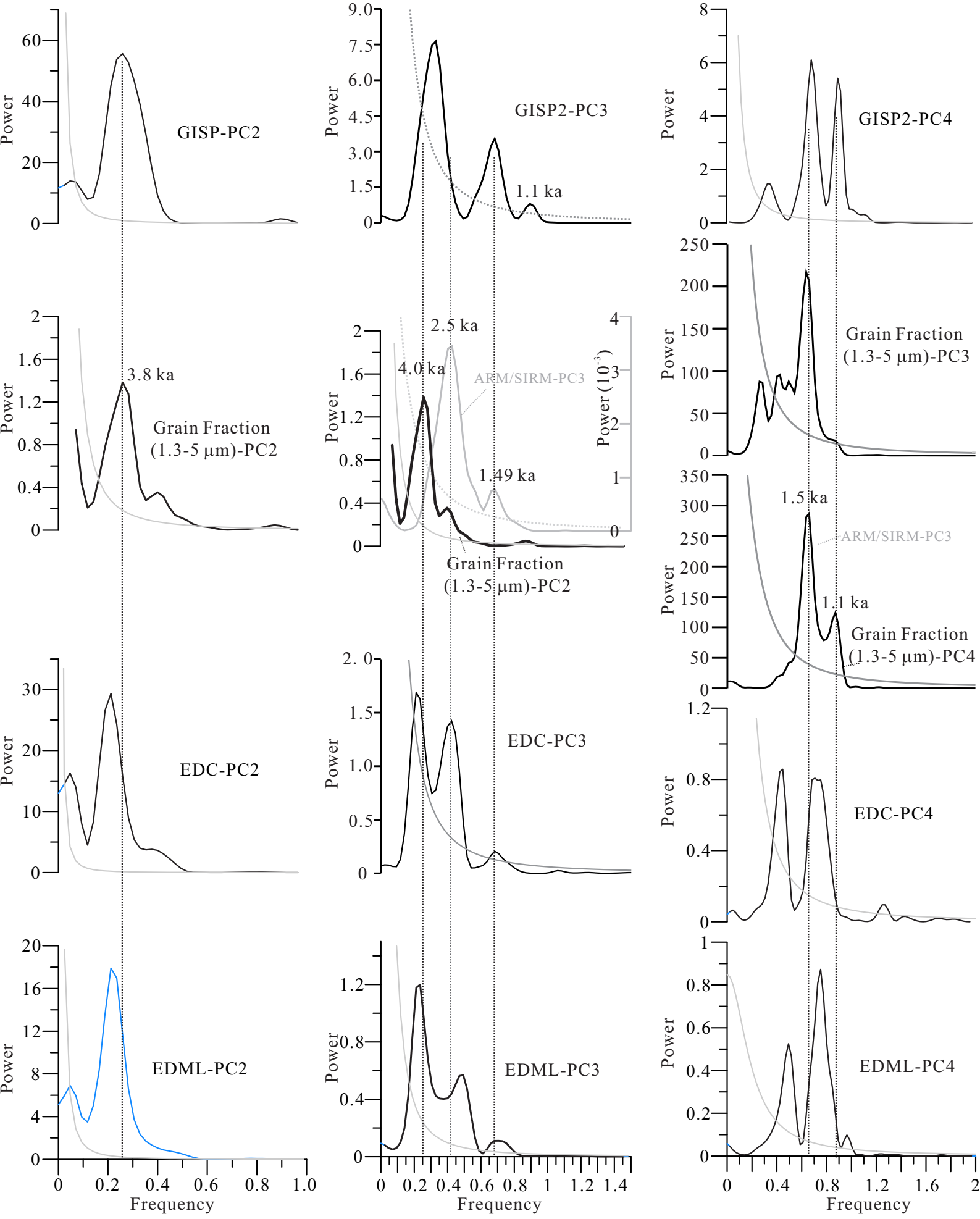
GISP-PC2
GISP2-PC3
1.1 ka
GISP2-PC4
3.8 ka
Grain Fraction
(1.3-5 μm)-PC2
2.5 ka
4.0 ka
ARM/SIRM-PC3
1.49 ka
Power (10-3)
Grain Fraction
(1.3-5 μm)-PC2
Grain Fraction
(1.3-5 μm)-PC3
1.5 ka
ARM/SIRM-PC3
1.1 ka
Grain Fraction
(1.3-5 μm)-PC4
EDC-PC2
EDC-PC3
EDC-PC4
EDML-PC2
EDML-PC3
EDML-PC4
Power
Frequency

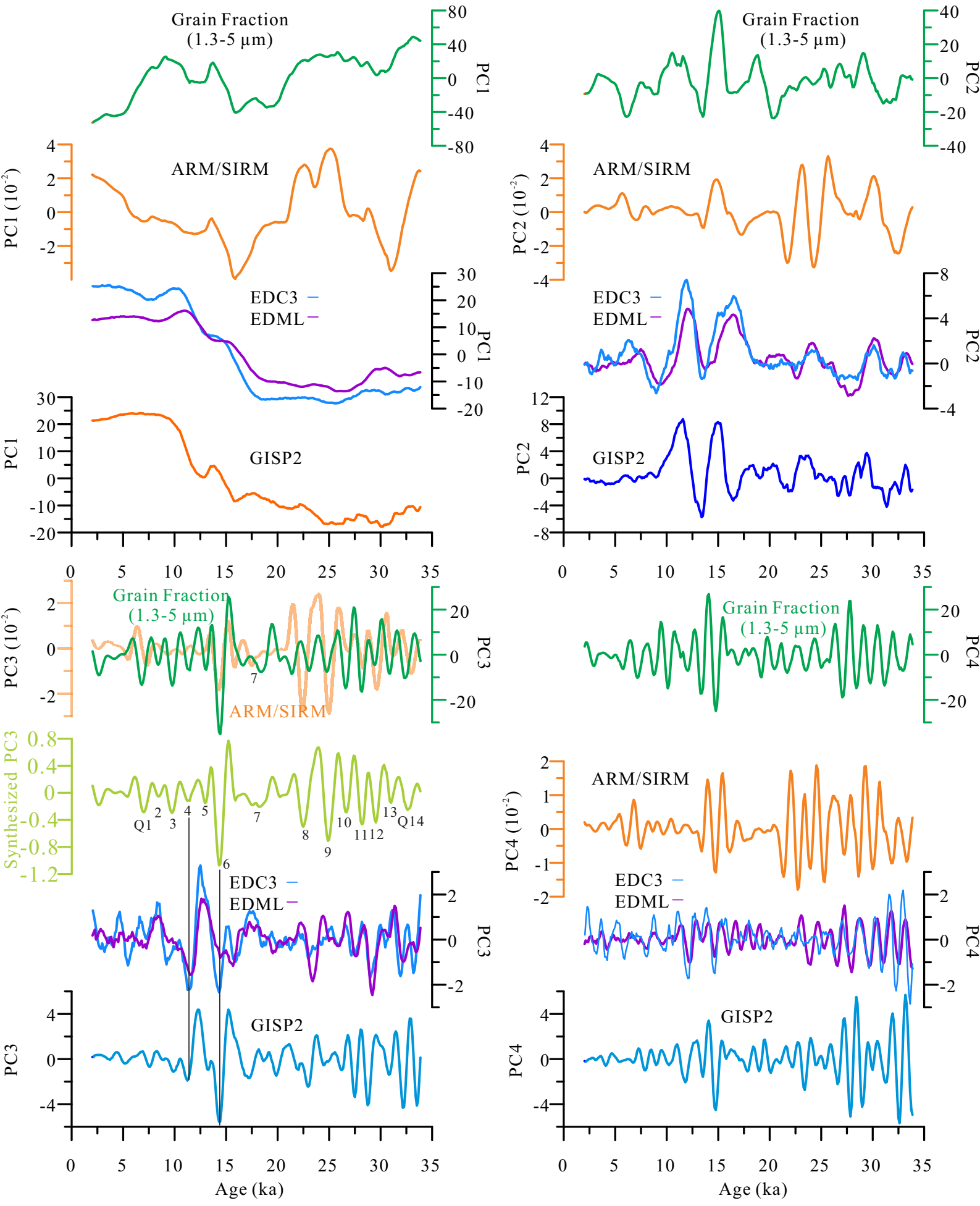
Grain Fraction
(1.3-5 μm)
PC1
ARM/SIRM
PC1 (10-2)
EDC3
EDML
PC1
GISP2
PC1
Grain Fraction
(1.3-5 μm)
PC2
ARM/SIRM
PC2 (10-2)
EDC3
EDML
PC2
GISP2
PC2
PC3 (10-2)
Grain Fraction
(1.3-5 μm)
ARM/SIRM
PC3
Grain Fraction
(1.3-5 μm)
PC4
Synthesized PC3
Q1
Q14
EDC3
EDML
PC3
GISP2
PC3
ARM/SIRM
PC4 (10-2)
EDC3
EDML
PC4
GISP2
PC4
Age (ka)
Age (ka)

Sample name	Depth（m）	Material dated	Conventional age (yr)	ERROR (yr)	2 Sigma Calibrated Max. (cal yr B.P.)	2 Sigma Calibrated Min. (cal yr B.P.)	Median probability (cal yr B.P.)
QH4C1-1	0.21	Leaves	1080	62.5	1055	930	990
QH4C1-2	0.74	Wood	5580	55	6410	6300	6360
QH4C1-4	1.37	Leaves	7520	35	8390	8320	8360
QH4C2-1	2.20	Plant material	11310	85	13255	13085	13170
QH4C2-2	3.05	twig	12630	120	15145	14905	15030
QH4C3-1	3.57	Bulk sediment	15790	120	19160	18920	19040
QH4C3-2	4.16	Wood	18140	155	22150	21840	22000
QH4C3-3	4.47	Plant material	20250	172.5	24490	24145	24320
QH4C3-4	5.15	Bulk sediment	24200	495	28475	27980	28230
QH4C4-1	5.78	twig	26760	115	31050	30820	30940
QH4-C4-2	6.69	Bulk sediment	28470	530	32940	31880	32410
QH4C5-1	7.40	Bulk sediment	31020	320	35250	34610	34930
QH4C5-2	7.97	twig	31170	382.5	35465	34700	35080

Table 1

AMS ^{14}C dating results